NAVAL POSTGRADUATE SCHOOL
Monterey, California

AD-A215 714

THESIS

LOCALIZATION OF MULTIPLE BROADBAND TARGETS
IN SPHERICAL COORDINATES VIA ADAPTIVE
BEAMFORMING AND NON-LINEAR ESTIMATION

by

Richard P. Breckenridge

June 1989

Thesis Advisor: Lawrence J. Ziomek

89 12

REPORT DOCUMENTATION PAGE

1a REPORT SECURITY CLASSIFICATION UNCLASSIFIED	1b RESTRICTIVE MARKINGS
2a SECURITY CLASSIFICATION AUTHORITY	3 DISTRIBUTION/AVAILABILITY OF REPORT APPROVED FOR PUBLIC RELEASE: DISTRIBUTION IS UNLIMITED.
2b DECLASSIFICATION/DOWNGRADING SCHEDULE	

4 PERFORMING ORGANIZATION REPORT NUMBER(S)	5 MONITORING ORGANIZATION REPORT NUMBER(S)

6a NAME OF PERFORMING ORGANIZATION NAVAL POSTGRADUATE SCHOOL	6b OFFICE SYMBOL (If applicable) 62	7a NAME OF MONITORING ORGANIZATION NAVAL POSTGRADUATE SCHOOL
6c. ADDRESS (City, State, and ZIP Code) MONTEREY, CA 93943-5000		7b. ADDRESS (City, State, and ZIP Code) MONTEREY, CA 93943-5000

8a. NAME OF FUNDING/SPONSORING ORGANIZATION	8b. OFFICE SYMBOL (If applicable)	9. PROCUREMENT INSTRUMENT IDENTIFICATION NUMBER

8c. ADDRESS (City, State, and ZIP Code)	10. SOURCE OF FUNDING NUMBERS			
	PROGRAM ELEMENT NO.	PROJECT NO.	TASK NO	WORK UNIT ACCESSION NO.

11 TITLE (Include Security Classification)
LOCALIZATION OF MULTIPLE BROADBAND TARGETS IN SPHERICAL COORDINATES VIA ADAPTIVE BEAMFORMING AND NON-LINEAR ESTIMATION.

12. PERSONAL AUTHOR(S)
BRECKENRIDGE, RICHARD P.

13a TYPE OF REPORT MASTER'S THESIS	13b TIME COVERED FROM _____ TO _____	14 DATE OF REPORT (Year, Month, Day) 1989, JUNE	15 PAGE COUNT 104

16 SUPPLEMENTARY NOTATION THE VIEWS EXPRESSED IN THIS THESIS ARE THOSE OF THE AUTHOR AND DO NOT REFLECT THE OFFICIAL POLICY OR POSITION OF THE DEPARTMENT OF DEFENSE OR THE U.S. GOVERNMENT.

17	COSATI CODES		18 SUBJECT TERMS (Continue on reverse if necessary and identify by block number)
FIELD	GROUP	SUB-GROUP	TARGET LOCALIZATION IN SPHERICAL COORDINATES, SONAR SIGNAL PROCESSING, FREQUENCY DOMAIN ADAPTIVE BEAMFORMING, NON-LINEAR LEAST-SQUARES ESTIMATION

19 ABSTRACT (Continue on reverse if necessary and identify by block number)

COMPUTER SIMULATION STUDIES OF TWO FREQUENCY DOMAIN ADAPTIVE BEAMFORMING ALGORITHMS FOR PLANAR ARRAYS ARE PRESENTED. THE ALGORITHMS ARE MODIFIED COMPLEX LMS ADAPTIVE ALGORITHMS THAT CAN PROCESS AN ARBITRARY NUMBER OF HARMONICS. THE ALGORITHMS PROVIDE ESTIMATES OF THE SPHERICAL COORDINATES (I.E., RANGE, DEPRESSION ANGLE, AND BEARING ANGLE) OF MULTIPLE BROADBAND TARGETS IN BOTH THE NEAR-FIELD AND FAR-FIELD. COMPUTER SIMULATION RESULTS COMPARING THE AVERAGE ESTIMATION ERROR FOR RANGE, DEPRESSION ANGLE, AND BEARING ANGLE AS A FUNCTION OF THE INPUT SNR, RANGE (NEAR-FIELD AND FAR-FIELD), AND HARMONIC NUMBER, ARE PRESENTED. THE "FULL ANGULAR COVERAGE" CAPABILITY OF THE ALGORITHMS WAS ALSO TESTED.

20 DISTRIBUTION/AVAILABILITY OF ABSTRACT ☑ UNCLASSIFIED/UNLIMITED ☐ SAME AS RPT ☐ DTIC USERS	21. ABSTRACT SECURITY CLASSIFICATION UNCLASSIFIED
22a NAME OF RESPONSIBLE INDIVIDUAL LAWRENCE J. ZIOMEK	22b TELEPHONE (Include Area Code) (408) 646-3206 22c OFFICE SYMBOL 62 Zm

DD FORM 1473, 84 MAR   83 APR edition may be used until exhausted
Λ other editions are obsolete

SECURITY CLASSIFICATION OF THIS PAGE

☆ U.S. Government Printing Office. 1986—606-24.

UNCLASSIFIED

LOCALIZATION OF MULTIPLE BROADBAND TARGETS IN
SPHERICAL COORDINATES VIA ADAPTIVE BEAMFORMING
AND NON-LINEAR ESTIMATION

by

Richard P. Breckenridge
Lieutenant, United States Navy
B.S., United States Naval Academy, 1982

Submitted in partial fulfillment of the
requirements for the degree of

MASTER OF SCIENCE IN ELECTRICAL ENGINEERING

and

MASTER OF SCIENCE IN ENGINEERING ACOUSTICS

from the

NAVAL POSTGRADUATE SCHOOL
June 1989

Author: _____
Richard P. Breckenridge

Approved by: _____
Lawrence J. Ziomek, Thesis Advisor

_____
James H. Miller, Second Reader

_____
John P Powers, Chairman Department of
Electrical and Computer Engineering

_____
Anthony A. Atchley, Chairman, Engineering
Acoustics Academic Committee

_____
Gordon E. Schacher, Dean of Science
and Engineering

ii

ABSTRACT

Computer simulation studies of two frequency domain adaptive beamforming algorithms for <u>planar arrays</u> are presented. The algorithms are modified complex LMS adaptive algorithms that can process an arbitrary number of harmonics. The algorithms provide estimates of the <u>spherical coordinates</u> (i.e., range, depression angle, and bearing angle) of <u>multiple broadband targets</u> in both the near-field and far-field. Computer simulation results comparing the average estimation error for range, depression angle, and bearing angle as a function of the input SNR, range (near-field and far-field), and harmonic number, are presented. The "full angular coverage" capability of the algorithms was also tested.

TABLE OF CONTENTS

I. INTRODUCTION

Frequency domain adaptive beamforming is a signal processing technique used to cophase the output electrical signals at each element in an array of sensors. The adaptive algorithm recursively adjusts the complex weights at each element in the array minimizing the mean-square-error between a reference signal and its estimate. The resulting steady-state phase weights represent the uncorrupted phase variation across the face of the array. The phase values at the elements in the array contain the location information of the source. Herein lies the usefulness of such an algorithm. By cophasing the output signals at each of the elements in a receive array using an adaptive beamformer, noise corruption that occurs in the medium and/or at the receiver can be effectively cancelled. The resulting steady-state phase values can be manipulated to determine the position of the source relative to the array. One obvious application for a beamformer of this nature is in determining the position of a sonar target in an ocean medium.

Target localization in bearing and depression angles has been successfully achieved using an adaptive beamformer of this design [Refs. 1, 2]. However, one localization parameter that is of significant interest and yet unsolved for by the previously mentioned signal processing algorithm [Refs. 1, 2]

1

is "target range." The objective of this thesis is to develop a localization algorithm that can process spherical wavefront information in a noise environment in order to determine the position of a target in range, bearing, and elevation. The frequency domain adaptive beamformer developed in [Refs. 1, 2] will be applied to this problem.

In our analysis, we modeled the target as a broadband sound source. As we convert a received output electrical signal to the frequency domain, the complex frequency spectrum of the target contains many frequency components. The frequency domain adaptive beamforming algorithm processes each spectral line of the target's signature independently. As a result, the target's position is estimated for each frequency component. Given a multi-target situation, the algorithm is capable of localizing each target provided that at least one unique spectral line can be associated with each sound source (target).

In Chapter II, we will develop the theoretical groundwork used in solving the localization problem. First, we consider the acoustical properties of wave propagation in an isospeed ocean medium. In Section II.A, we begin with a general form of the inhomogeneous wave equation and develop the output electrical signals at each of the elements in a planar array. Based on a given signal-to-noise ratio (SNR), we corrupt the output electrical signals with noise. This time-domain signal is converted to the frequency domain for processing (Sec.

II.B). The signal is filtered using a frequency domain, modified least-mean-squares (LMS) adaptive algorithm. Since we are analyzing spherical waves, this routine has been modified to include analysis that assumes non-separable complex weights. Other phase distortions introduced by the signal processing routine are cancelled using techniques discussed in the remainder of Section II.B. The last section of Chapter II presents an algorithm that was developed to process the complex weights in order to determine the position of the target in spherical coordinates.

In Chapter III, several computer simulation studies are discussed. The test cases were selected in order to demonstrate the significant properties of the localization algorithm. In each case, the run was first conducted in a noise-free environment to validate the propagation and localization models. Once the baseline results were generated, the test cases were repeated in a noise environment.

Section III.A tests the full angular coverage capability of the algorithm. Full angular coverage implies that the target can be localized regardless of its relative position to the receive array. A single target is placed at a broadside and then endfire position relative to the array. The range of the target is then varied to determine the performance of the algorithm in the near and far-field regions. One additional test case placing the target at an

3

arbitrary geometry relative to the array is also examined in this section. In Section III.B, the multi-harmonic capability of the algorithm is exercised. The test case reviews the performance of the algorithm given a single target with several harmonics, covering a wide frequency spectrum. In the final section of our results chapter, Section III.C, we examine the multi-target performance of the algorithm. In this simulation study, three targets with different locations are tested. The final conclusions and recommended areas for further research are presented in Chapter IV.

II. THEORETICAL DEVELOPMENT

The purpose of this chapter is to present the theoretical groundwork used in solving the localization problem. The approach can be divided into three major areas (see Figure 2.1). In generating the output electrical signals at the elements in the receive array, we first consider the acoustical nature of the problem. Beginning with a general form of the wave equation, we derive a mathematical model for spherical wave propagation in a homogeneous medium. The wave propagation model is used to generate both the input acoustic signals and the output electrical signals at the transducers in the array. Based on a given signal-to-noise ratio (SNR),
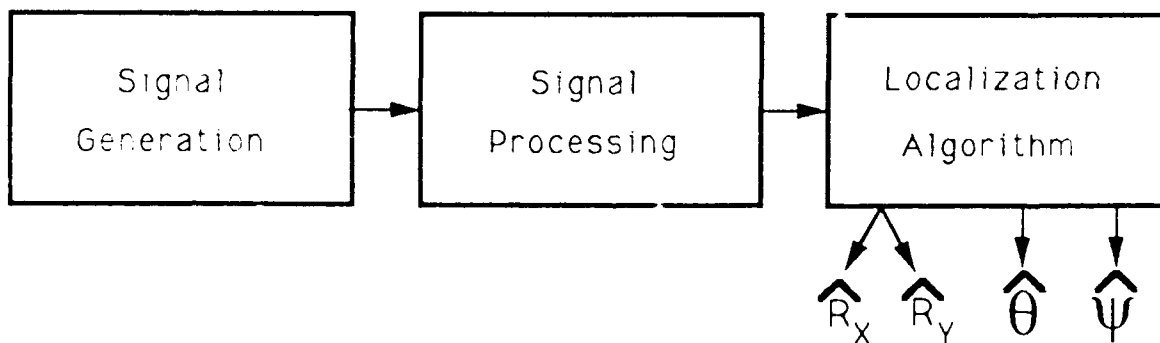
Figure 2.1   The Block Diagram Representation of the Analysis
Steps Used in Solving the Localization Problem.

the output electrical signals are corrupted by noise. Using a frequency-domain adaptive beamformer, the output signals from the elements in the receive array are co-phased. The steady-state phase weights determined by the beamformer are then processed by a localization algorithm that provides an estimate of the target's position in spherical coordinates.

A. SIGNAL GENERATION

The starting point of the localization problem is the generation of the acoustic signal incident on the planar array. The signal must represent wave propagation in an isospeed ocean medium. Specifically, our signal must exhibit spherical wavefront curvature that is a function of the range between the source and the array. This mathematical signal model is developed by solving the wave equation. The corresponding output electrical signals are then discretized by taking a preset number of time samples over the data record length at each element. The final step of signal generation is to add noise to the electrical signals. The output from this section is a time-domain, noise-corrupted signal at each transducer element in the receive array (see Figure 2.2).

1. Spherical Wave Propagation Model

The propagation of acoustic energy in the ocean can be described by the following inhomogeneous wave equation:

$$\nabla^2 \varphi(t, r) - \frac{1}{c^2(r)} \frac{\partial^2}{\partial t^2} \varphi(t, r) = x_M(t, r) \qquad (2.1)$$
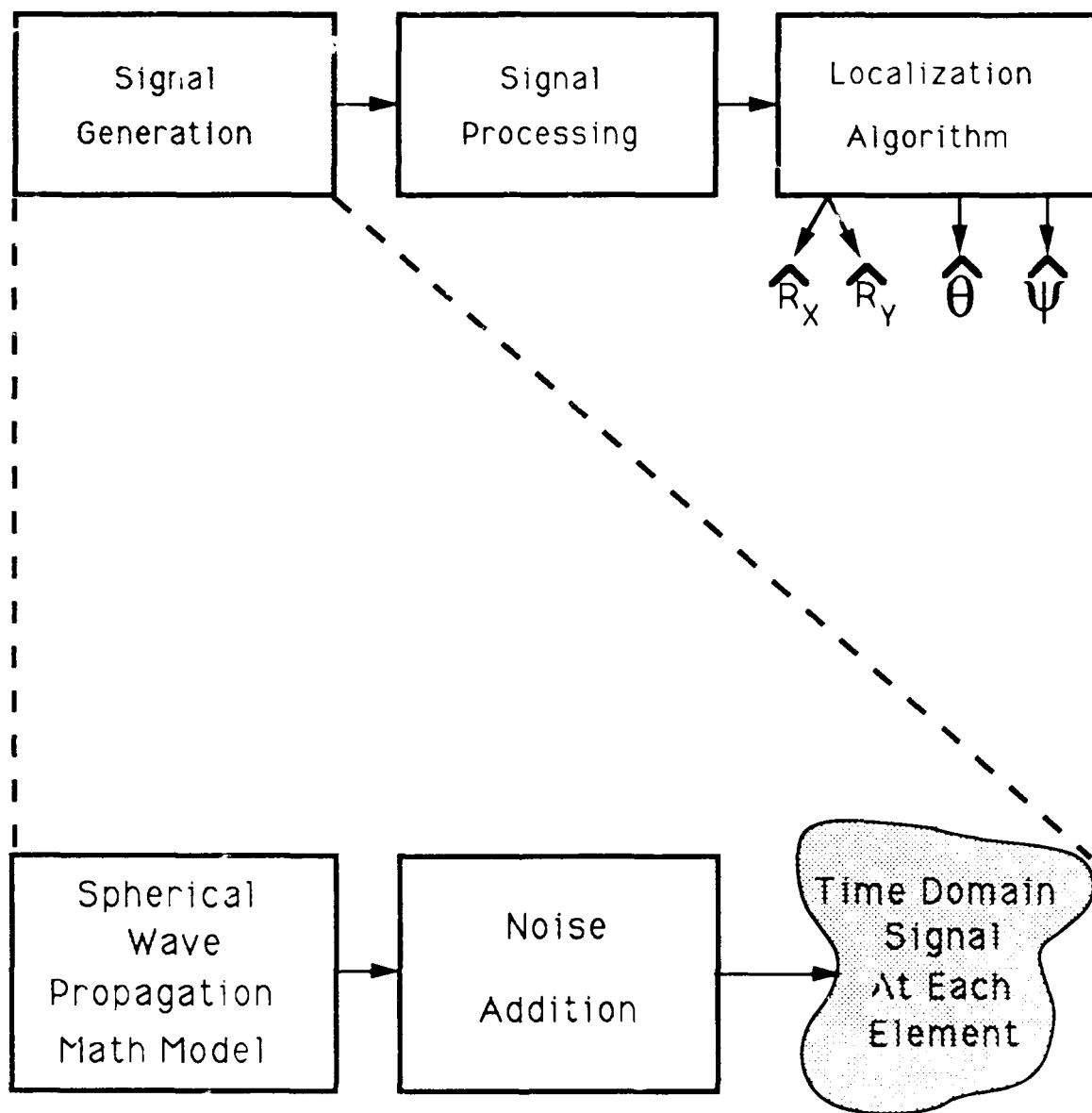
Figure 2.2   The Block Diagram Representation of the Major
Steps Performed in Signal Generation.

where $\varphi(t,r)$ is the velocity potential at time t and position r, $x_M(t,r)$ represents the source distribution, and $c(r)$ is the speed of sound in the ocean. In our problem, we are interested in wave propagation in a homogeneous medium. Therefore, $c(r)$ is set equal to a constant sound speed c. When the speed of sound is constant, the solution to the wave Equation (2.1) is given by:

$$\varphi(t,r) = -\frac{1}{4\pi} \int_{V_0} \frac{x_M\left(t - \left(\frac{|r - r_0|}{c}\right), r_0\right)}{|r - r_0|} \, dV_0 \qquad (2.2)$$

where $|r - r_0|$ is shown in Figure 2.3 [Ref. 3:p. 286].

Next, we model the source distribution generated by the target as an omnidirectional point source with arbitrary time dependence located at $r = r_o$ (see Figure 2.3). That is, let

$$x_M(t,r) = g(t)\, \delta(r - r_0) \qquad (2.3)$$

where g(t) is an arbitrary function of time. By substituting Equation (2.3) into Equation (2.2) and performing the integration, the velocity potential $\varphi(t,r)$, reduces to

$$\varphi(t,r) = -\frac{g\left(t - \frac{R}{c}\right)}{4\pi R} \qquad (2.4)$$
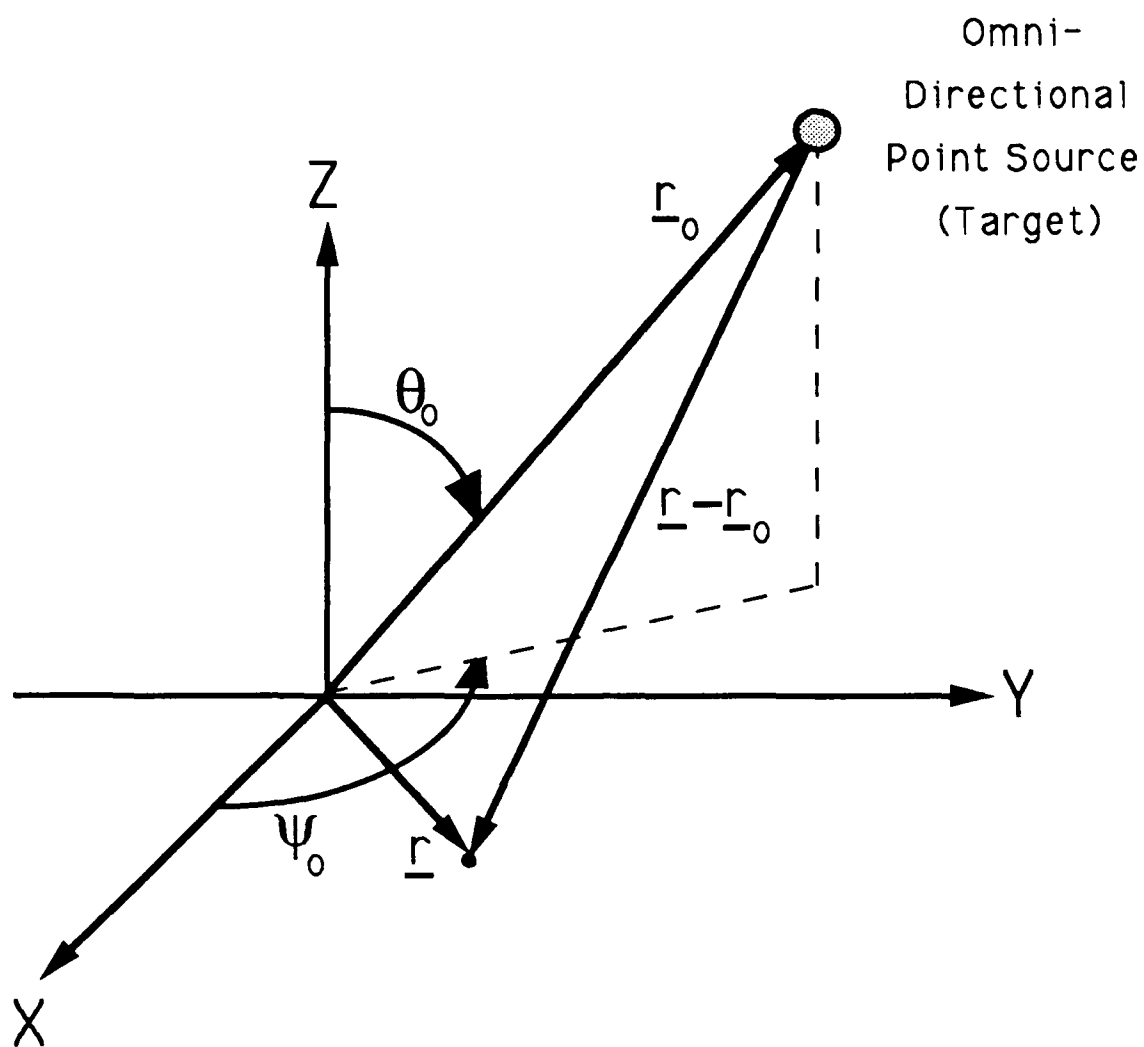
Figure 2.3 Spherical Coordinates $r_0 = |\mathbf{r}_0|$, θ_0, and, ψ_0 defining the Position of the Target.

where

$$R = | \mathbf{r} - \mathbf{r}_0 |. \tag{2.5}$$

As a result, we can express the acoustic signal $y_M(t, \mathbf{r})$ incident upon the array [Ref. 4] as

$$y_M(t, \mathbf{r}) = \frac{g\left(t - \dfrac{R}{c}\right)}{R}. \tag{2.6}$$

At this point, we can apply the physical conditions of our array to this general expression of the input acoustic signal Equation (2.6). First, we shall assume that the output electrical signal $y(t, \mathbf{r})$ is directly proportional to the input acoustic signal, that is,

$$y(t, \mathbf{r}) = y_M(t, \mathbf{r}) \tag{2.7}$$

where the constant of proportionality has been dropped. Next, we will sample this continuous electrical signal at a sampling rate f_s, providing a discrete form of the time-domain signal in preparation for signal processing. Consider a planar array lying in the XY plane. Given the interelement spacings of the array d_x and d_y, the element position vector $\mathbf{r}$ (see Figure 2.3) can be expressed as

$$\mathbf{r} = m d_x \, \widehat{x} + n d_y \, \widehat{y}, \quad z = 0. \tag{2.8}$$

10

The location of the source as measured from the center of the array $\mathbf{r}_o$ is

$$\mathbf{r}_0 = x_0 \hat{x} + y_0 \hat{y} + z_0 \hat{z}. \tag{2.9}$$

Therefore, the magnitude of the range to the target, R, can be expressed as

$$R = | \mathbf{r} - \mathbf{r}_0 | = \left[\left(md_x - x_0 \right)^2 + \left(nd_y - y_0 \right)^2 + z_0^2 \right]^{1/2}. \tag{2.10}$$

By taking L time samples over the record length, the discrete representation of the signal is

$$y\left(lT_s, md_x, nd_y \right) = \frac{g\left(lT_s - \frac{R}{c} \right)}{R} \tag{2.11}$$

where "l" corresponds to a particular time instant and

$$T_s = \frac{1}{f_s} \tag{2.12}$$

is the sampling period.

The arbitrary function of time g(t) is represented by the following finite Fourier series:

$$g(t) = a_0 + 2 \sum_{q=1}^{K} a_q \cos \left(2\pi q f_0 t + \theta_q \right), \tag{2.13}$$

11

where: a_0 is the DC component of the source signal,

a_q is the magnitude of the Fourier series coefficient

of the source signal at harmonic q,

Θ_q is the phase of the Fourier series coefficient of

the source signal at harmonic q,

f_0 is the fundamental frequency of the source signal,

and   K   is the total number of harmonics.

By setting time t in Equation (2.13) equal to the retarded time $\left(lT_s - \dfrac{R}{c} \right)$ and substituting this equation into Equation (2.6), we obtain the final form of the output electrical signal at the receive array:

$$y\left(lT_s, md_x, nd_y \right) = \frac{1}{R}\left\{ a_0 + 2\sum_{q=1}^{K} a_q \cos\left[2\pi q f_0 \left(lT_s - \frac{R}{c} \right) + \Theta_q \right] \right\}. \quad (2.14)$$

2.   Noise Addition

To validate the signal processing and localization algorithms, as well as our wave propagation model used in generating the signals, we first perform the analysis in a noise-free environment.   However, once the baseline results have been obtained, we must test the performance of the overall algorithm under realistic environmental conditions. Therefore, we corrupt the output signal at each element in the array with noise.   Additive, zero mean, white, Gaussian noise is added to the output signals from each element in the

planar array. We select various signal-to-noise ratio (SNR) values to simulate a particular noise environment. The resulting signals represent discrete time, noise corrupted, output signals at each element in the planar array.

B. FREQUENCY DOMAIN SIGNAL PROCESSING

The output signal at each of the transducer elements is converted to the frequency domain by using a Discrete Fourier Transform (DFT) routine. In this section, we will begin our discussion by deriving the form of the radiated signal after taking the DFT. Next, we will examine all phase components that surface in our frequency-domain analysis. Common terms associated with wavefront curvature will then be presented.

The frequency-domain signal processing routine can be divided into three major functions (see Figure 2.4). The modified least-mean-squares (LMS) adaptive algorithm will be the first topic of discussion. By cophasing the output signals from the elements in the array to yield a minimum least-squares error, the noise corruption of the signal is reduced. Another source of phase distortion occurs in the conversion to the frequency domain. The phase values calculated by taking the DFT are limited to a closed interval between $[-\pi, \pi]$. This phase "wrapping" effect must be rectified prior to further processing by the localization algorithm. This effect is corrected by the phase unwrapping algorithm. The "unwrapped", steady-state phase weights are

13

Signal Generation

Signal Processing

Localization Algorithm

$\hat{R}_X$ $\hat{R}_Y$ $\hat{\theta}$ $\hat{\psi}$

D F T

LMS Adaptive Algorithm

Phase Unwrapping Algorithm

Non-Linear Least Squares Estimation

Frequency Domain Signal Processing
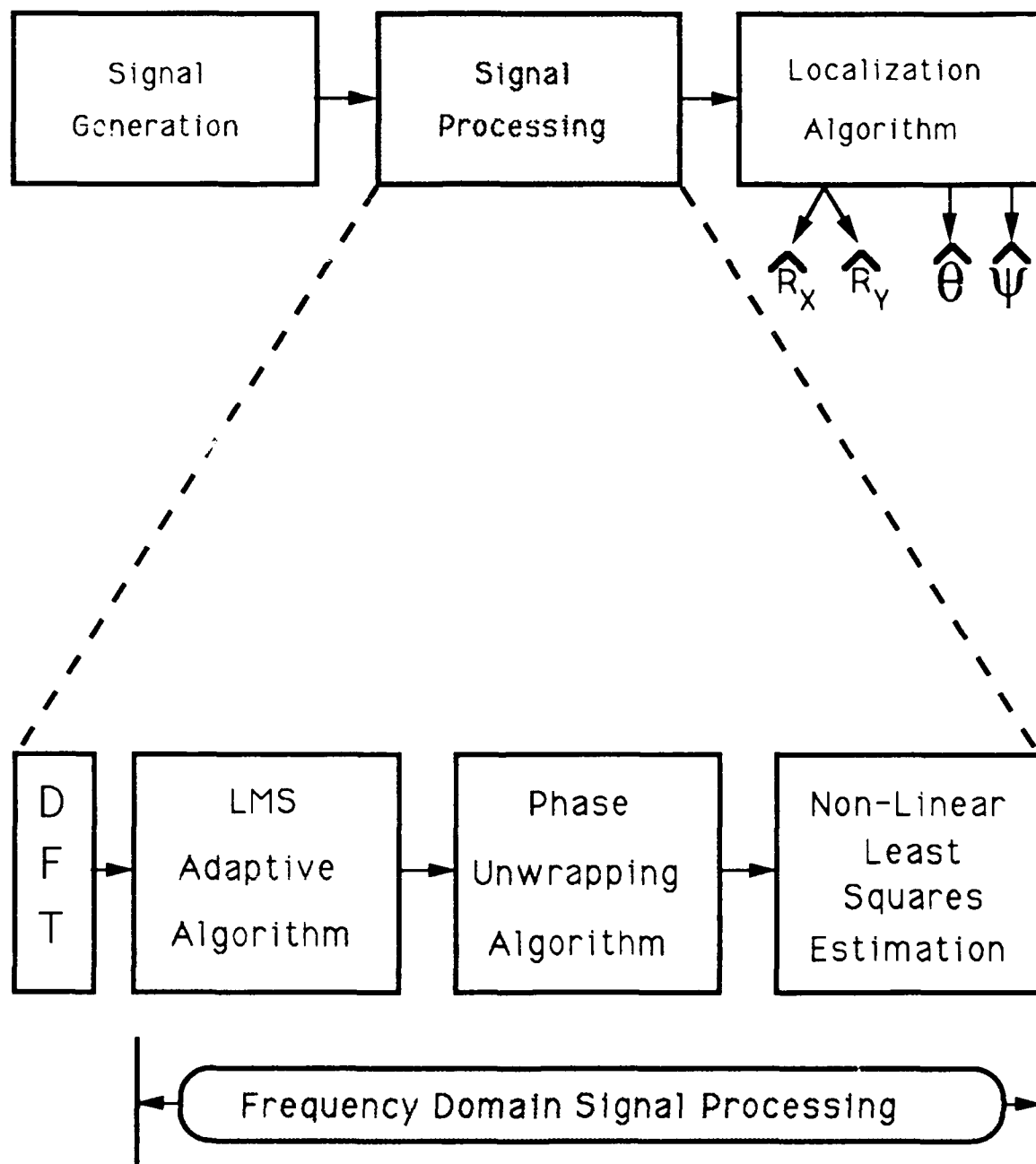
Figure 2.4   Block Diagram Representation of the Major Steps Performed in Signal Processing.

then smoothed along the X and Y axes using non-linear least-squares estimation. The output from this signal processing section is an estimate of the uncorrupted phase at each element in the receive array.

1. **Phase Components Encountered in Frequency Domain Analysis**

From our analysis in Section II.A.1, we developed a discrete, time-domain expression of the output electrical signal at each of the elements in the planar array. As in most signal processing applications, it is often more convenient to operate on the signal in the frequency domain. Therefore, our first manipulation is to take the DFT of the signal. The sampled output spectrum, $Y_s(q,m,n)$, is given by

$$Y_s(q,m,n) = c_{mn} \sum_{l=-L'}^{L'} y\left(lT_s, md_x, nd_y\right) e^{-j2\pi ql/L}, \qquad q = 1, 2, \ldots, K \qquad (2.15)$$

where
$$L' = (L-1)/2 \qquad (2.16)$$

and c_{mn} is the complex weight at each element (m,n). Substituting Equation (2.11) into Equation (2.15) yields

$$Y_s(q,m,n) = \frac{c_{mn}}{R} \sum_{l=-L'}^{L'} g\left(lT_s - \frac{R}{c}\right) e^{-j2\pi ql/L}, \qquad q = 1, 2, \ldots, K \qquad (2.17)$$

15

The Fourier series coefficients introduced to represent the arbitrary function of time g(t) in Equation (2.13) can be expressed by the following complex coefficients, c_q:

$$c_q = a_q e^{j\theta_q}, \qquad q = 1, 2, \ldots, K \qquad\qquad (2.18)$$

where a_q is the magnitude and θ_q is the phase of harmonic q. Since the Fourier series coefficients c_q represent g(t), then we know from the properties of Fourier series that $g(t \pm t_o)$ will have the Fourier series coefficients $c_q e^{\pm j 2\pi q f_0 t_0}$. Therefore, Equation (2.17) can be written in the following simplified form [Ref. 5:pp. 162-166]

$$Y_s(q,m,n) = \frac{L}{R} c_{mn} c_q e^{-j 2\pi q f_0 R/c}, \qquad q = 1, 2, \ldots, K \qquad (2.19)$$

where R/c is substituted for t_o. The range R is given by Equation (2.5) as the magnitude of the vector   , which is the range from a particular element in the array to the target (see Figure 2.3). Using vector algebra, this magnitude can be rewritten as

$$\left| \mathbf{r} - \mathbf{r}_0 \right| = \left[\left(\mathbf{r} - \mathbf{r}_0 \right) \bullet \left(\mathbf{r} - \mathbf{r}_0 \right) \right]^{1/2} . \qquad\qquad (2.20)$$

By expanding the dot product within the radical, R can be rewritten as

16

$$\left| \mathbf{r} - \mathbf{r}_0 \right| = \left[r_0^2 - 2r_0 \left(\hat{a}_{r_0} \cdot \mathbf{r} \right) + r^2 \right]^{1/2} \tag{2.21}$$

where
$$\hat{a}_{r_0} = u_0 \hat{x} + v_0 \hat{y} + w_0 \hat{z} \tag{2.22}$$

is the unit vector in the direction of $\mathbf{r}_o$, and is defined in terms of direction cosines u_o, v_o, and w_o as follows (see Figure 2.3):

$$u_0 = \sin \theta_0 \, \cos \psi_0 \tag{2.23}$$

$$v_0 = \sin \theta_0 \, \sin \psi_0 \tag{2.24}$$

and
$$w_0 = \cos \theta_0 . \tag{2.25}$$

By taking the dot product of Equation (2.8) with Equation (2.22), and substituting the result into Equation (2.21) we obtain:

$$\left| \mathbf{r} - \mathbf{r}_0 \right| = \left[r_0^2 - 2r_0 \left(u_0 m d_x + v_0 n d_y \right) + \left(m d_x \right)^2 + \left(n d_y \right)^2 \right]^{1/2} . \tag{2.26}$$

From this range expression and by referring back to Equation (2.19), we can define the phase term due to the propagation of acoustic energy from the source as

$$\theta_r \equiv -\frac{2\pi q f_0}{c} \left[r_0^2 - 2r_0 \left(u_0 m d_x + v_0 n d_y \right) + \left(m d_x \right)^2 + \left(n d_y \right)^2 \right]^{1/2} . \tag{2.27}$$

17

This term, θ_r, is the phase due to source *radiation* and contains the physical localization information of the target. By solving for r_o, u_o, and v_o, we can determine the spherical coordinates of the source.

At this point in our discussion it is proper to introduce all of the other phase components that exist at a given transducer element in the receive array. Beginning at the source, the first phase term that we have discussed is due to the physical propagation of acoustic energy, θ_r. Additionally, another phase term exists that originates from the target. The source signal also contains an initial phase term at each harmonic. Specifically, we defined this in Equation (2.12) as the phase of the Fourier coefficient, θ_c. Since this phase is not known a priori from the localization side of the problem, we must solve for this unknown in order to obtain the radiation phase term, θ_r. Our objective in this section is to develop an approximation of the uncorrupted signal phase and to pass this output

$$\theta_{sig} = \theta_r + \theta_q \qquad (2.28)$$

to the localization algorithm (see Section II.C).

Three other phase terms exist that distort the signal phase mentioned above. We can represent the noise corruption

18

of the input acoustic signal by a phase term, θ_n. This phase term varies at each element and for each harmonic analyzed. The objective of the LMS adaptive algorithm is to cancel this noise phase term at each element. Another source of phase distortion occurs in the conversion to the frequency domain. The phase values calculated by taking the DFT are limited to a closed interval between $[-\pi, \pi]$. When a phase value exceeds the interval of $[-\pi, \pi]$, the phase is "wrapped" within the limits of the interval by adding/subtracting 2π. This phase "wrapping" effect can be accounted for by the term θ_{wrap}. The function of the "phase unwrapping algorithm" is to unwrap the phases at the elements along the X and Y axes. Lastly, a constant phase term is added to the phase at each element in the array as a result of the cophasing process of the LMS adaptive algorithm. This phase term, θ_c, is not cancelled by the signal processing routine of this section. The phase term θ_c is passed along with the estimate of $\theta_{?}$ to the localization algorithm. This algorithm groups the θ_c term with the θ_q component, and cancels them both yielding the θ_r term. In summary, the total phase component at a particular element can be described by the following equation:

$$\theta_{tot} = \theta_r + \theta_q + \theta_n + \theta_{wrap} + \theta_c . \qquad (2.29)$$

19

2. <u>Common Terms Associated with Wavefront Curvature</u>

A wavefront is defined as a surface of constant phase. Figure 2.5 depicts two sound sources (targets) located at broadside relative to a planar array. The target shown in Figure 2.5.a is located close to the receive array. Looking at the incident wavefront on the surface of the array, we observe significant wavefront curvature. When a wavefront, as measured at the receive array, exhibits significant curvature, the target is considered to be in the "near-field (NF)". Figure 2.5.b shows the same target at a more distant position from the array. The amount of wavefront curvature seen at the array face is noticeably less. If a wavefront has slight curvature or resembles a plane wave, the target is considered to be in the "far-field (FF)". One observation that can be made from this figure is that the range information of a target's position can be found in the curvature of the wavefront. The range to the physical boundary between the near-field and far-field regions is a function of the array size and the wavelength of the incident acoustic field (see Figure 2.6) and is given by [Ref. 5:p. 33]

$$\rho = \frac{\pi R_{array}^2}{\lambda} \qquad (2.30)$$

where ρ is the range to the NF/FF boundary, R_{array} is the effective radius of the array, and λ is the wavelength of
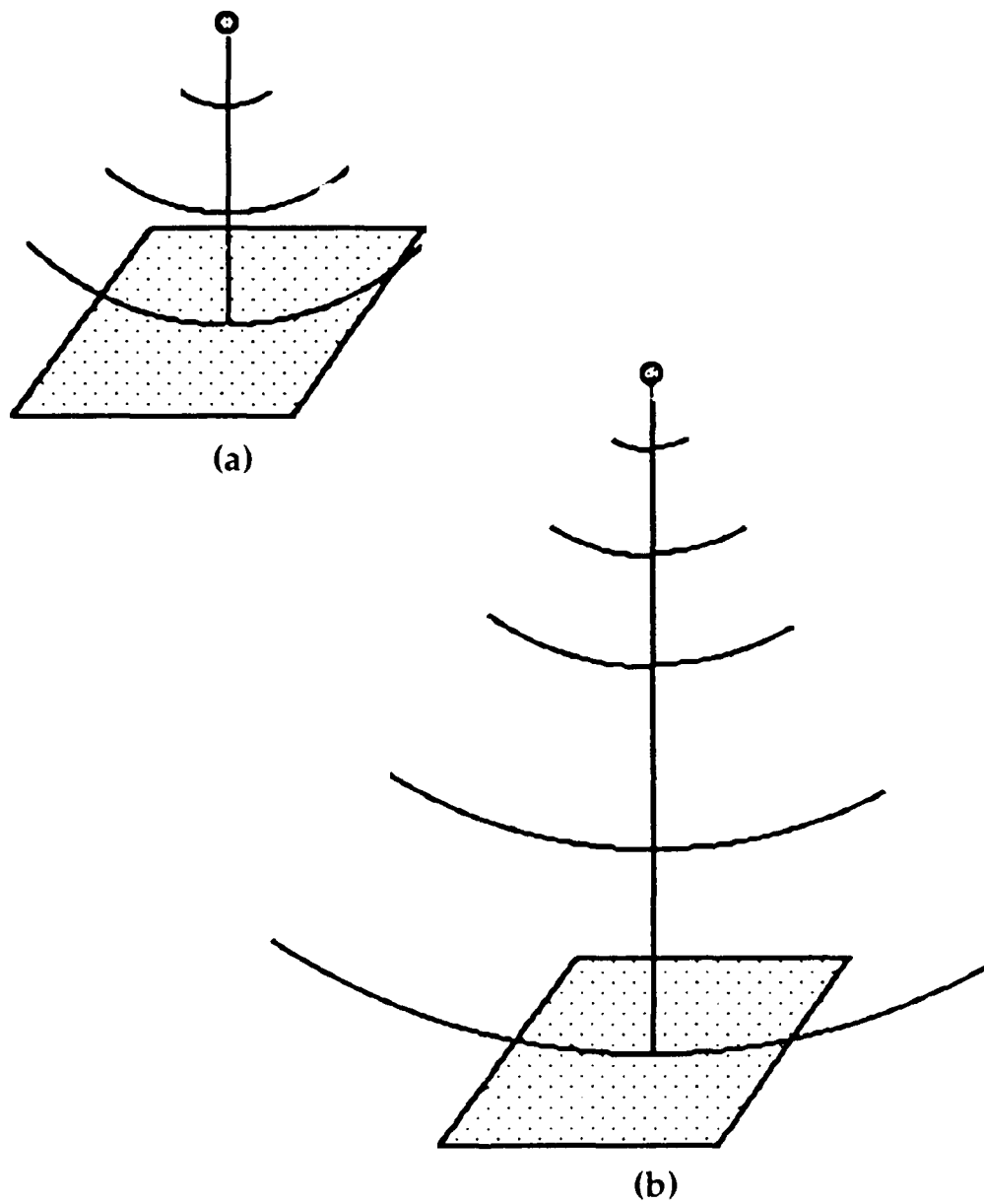
Figure 2.5 Representation of the Range Effects
on Wavefront Curvature.
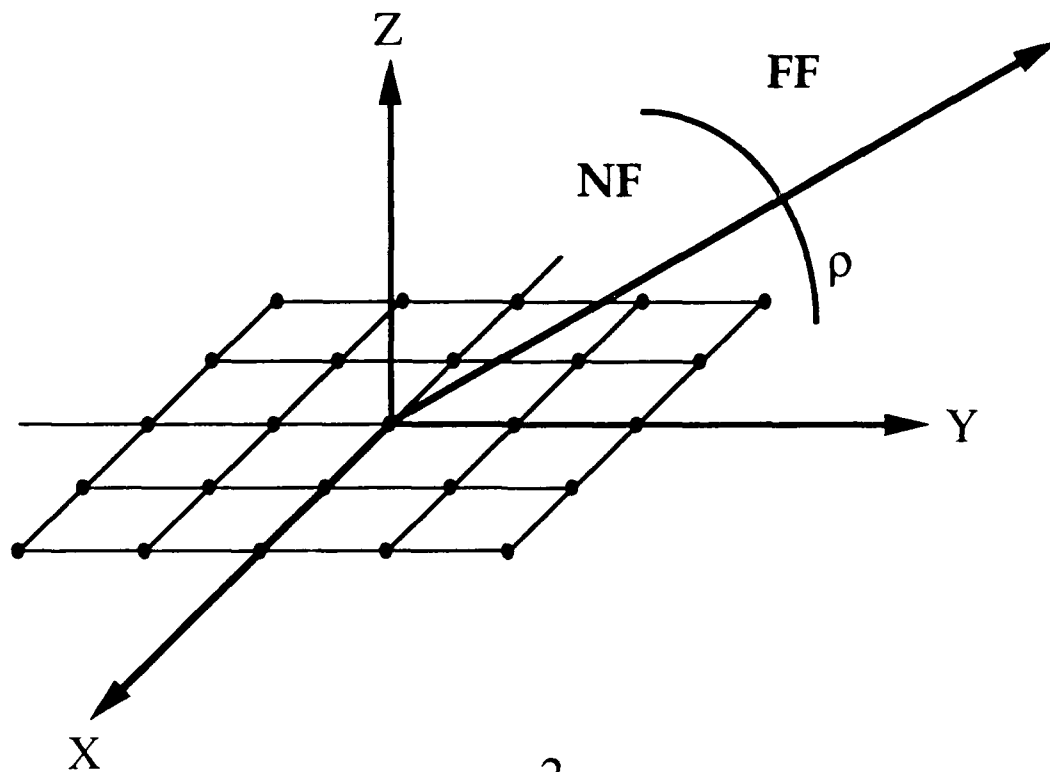
$$\rho = \frac{\pi R_{array}^2}{\lambda}$$

$$r \overset{NF}{\underset{FF}{\lessgtr}} \rho$$

Figure 2.6   Representation of Near-Field/ Far-Field Boundary.

the incident field. By considering a rectangular array of M × N elements, Equation (2.30) becomes

$$\rho = \frac{\pi}{\lambda}\left[\left(L_x/2\right)^2 + \left(L_y/2\right)^2\right] \qquad (2.31)$$

where

$$L_x = (M-1)d_x \qquad (2.32)$$

$$L_y = (N-1)d_y \qquad (2.33)$$

$$d_x = d_y = \lambda_{min}/2 \qquad (2.34)$$

and

$$\lambda_{min} = c/f_{max}. \qquad (2.35)$$

Given a target with K_{max} harmonics, f_{max} is equal to the total number of harmonics, K_{max}, times the fundamental frequency, f_o, that is

$$f_{max} = K_{max}f_0. \qquad (2.36)$$

Since the broadband signal of the target can encompass a wide range of frequencies, one unique value for ρ that delineates the boundary between the near and far fields does not exist. Rather, one can only specify a unique NF/FF boundary for a given harmonic of interest due to the frequency dependence of the range, ρ. However, a target can be classified as a near-field target at all harmonics provided that it is located within a minimum ρ value defined in terms of the maximum wavelength as follows:

$$\rho_{min} = \frac{\pi}{\lambda_{max}} \left[\left(L_x/2 \right)^2 + \left(L_y/2 \right)^2 \right]. \qquad (2.37)$$

Conversely, if a target's range is greater than a maximum ρ value, it is classified as a far-field contact for all harmonics, where

$$\rho_{max} = \frac{\pi}{\lambda_{min}} \left[\left(L_x/2 \right)^2 + \left(L_y/2 \right)^2 \right]. \qquad (2.38)$$

This NF/FF boundary is a helpful tool in classifying the relative target position to the array since it takes into account array size and target frequency components. One misconception that has resulted from establishing a boundary of this nature is the argument that only targets located in the near-field can be localized in range. Although it is true that a near-field target has significant wavefront curvature, our research demonstrates that an adequate range estimate can be determined given a wave with a slight amount of wavefront curvature (i.e., for targets located well into the far-field).

At the beginning of this section, we defined a wavefront as a surface of constant phase. Using the phase information at the elements of the planar array, another way in which wavefront curvature can be defined is by plotting the phase as a function of element position across the X and Y axes. For a near-field target, this phase distribution will exhibit significant curvature. The phase distribution across

24

either the X or Y axis of the array for a far-field target will be more linear. In the results section, we will plot the ideal phase distribution across these two array axes for each of the cases that we analyze.

3. Least-Mean-Squares (LMS) Adaptive Algorithm

As discussed in the previous section, the phase passed to the frequency-domain modified LMS adaptive algorithm for processing is comprised of many components. The measured phase, θ_m, can be described by

$$\theta_m = \theta_r + \theta_q + \theta_n + \theta_{wrap}. \tag{2.39}$$

The objective of the adaptive algorithm is to cancel out the noise term, θ_n. The algorithm performs this function by adaptively updating the complex weights at each element in the array while attempting to minimize the mean-square error.

The LMS adaptive algorithm is a well known signal processing aid [Ref. 6]. In recent research work [Ref. 1], a frequency-domain modified LMS adaptive algorithm was applied to a planar array to process plane-wave signals. Specifically, complex weights at each element in the array were optimized adaptively with respect to a reference signal. The ideal value of the phase of each complex weight is equal to the negative value of the uncorrupted wrapped signal phase. The algorithm used for this plane wave case assumed that the complex weights were separable. This is a valid assumption

25

for plane-wave analysis or cases when the wavefront curvature is minimal (i.e., far-field problems). However, for those cases with significant wavefront curvature and a resulting interdependence between x and y coordinates, this assumption is not valid.

The following equations summarize the key steps that comprise the adaptive algorithm assuming separable complex weights [Ref. 2]. For the remainder of the thesis, this algorithm will be called LMS_{flat}, where the word "flat" implies negligible curvature.

Estimate: $$\hat{z}_i(q) = \frac{1}{LMN} \sum_n d_i(q,n) \sum_m c_i(q,m) \, Y(q,m,n) \qquad (2.40)$$

where $\hat{z}_i(q)$ is the estimate of the reference signal at harmonic q at the ith iteration and where the complex weights c_{mn} are assumed to be separable, that is,

$$c_{mn}(q) = c(q,m) \, d(q,n) \qquad (2.41)$$

Error Signal: $$e_i(q) = z(q) - \hat{z}_i(q) \qquad (2.42)$$

Complex Weight Update:

$$c_{i+1}(q,m) = c_i(q,m) + 2\mu_i(q) e_i(q) \left(\sum_n d_i(q,n) \, Y(q,m,n) \right)^* \qquad (2.43a)$$

$$d_{i+1}(q,n) = d_i(q,n) + 2\mu_i(q) e_i(q) \left(\sum_m c_i(q,m) \, Y(q,m,n) \right)^* \qquad (2.43b)$$

26

$$\mu_i(q) = \frac{1}{\left[\frac{1}{L}|Y(q,0,0)|\right]^2}$$

where

(2.43c)

is the step size parameter. The adaptive routine computes Equations (2.40) through Equations (2.43c) N times, minimizing the error signal e_i. After each iteration, the magnitude of the complex phase weights $c_{i+1}(q,m)$ and $d_{i+1}(q,n)$ are normalized in order to maintain unit magnitude. By normalizing the magnitude of the phase weights after each iteration, the phase component of the phase weights is the term that is recursively optimized to minimize least-squares error. With this modification, the final output from the algorithm is a set of steady-state, phase weights that represent the negative values of the uncorrupted wrapped phase of the output electrical signal at each element in the array.

The adaptive algorithm summarized above (derived in [Ref. 2]) was modified to process near-field waves (i.e., waves with significant wavefront curvature) by expressing the complex weights in a non-separable form. This algorithm will be referred to as LMS_{curve} where the word "curve" implies significant curvature. The complex weights c_{mn} are set equal to $w(m,n)$ in these equations:

Estimate:

$$\hat{z}_i(q) = \frac{1}{LMN}\sum_m \sum_n w_i(q,m,n)\, Y(q,m,n)$$

(2.44)

Error Signal:

$$e_i(q) = z(q) - \hat{z}_i(q)$$

(2.45)

27

Complex Weight Update:

$$w_{i+1}(q,m,n) = w_i(q,m,n) + 2\mu_i(q)e_i(q)Y^*(q,m,n) \qquad (2.46)$$

where $\mu_i(q)$ is defined in Equation(2.43c). As in the LMS_{flat} algorithm, the magnitude component of the complex phase weights is normalized to unity after each iteration.

In summary, adaptive algorithm LMS_{flat} assumes that the complex weights are separable and will work best for cases with minimal wavefront curvature. LMS_{curve} assumes non-separable weights and will give better performance for cases with significant wavefront curvature. In the results section, both algorithms have been used for each scenario presented to demonstrate these properties of the two algorithms.

4. **Phase Unwrapping Algorithm**

The output from the two LMS adaptive algorithms are processed sets of steady-state, "wrapped" phase values of the output electrical signals at each element in the array. As mentioned earlier, phase distortion occurs in the conversion to the frequency domain. The phases calculated by the DFT are limited to a closed interval between $[-\pi,\pi]$. As a phase value exceeds this interval, the phase is "wrapped" within the limits of $[-\pi,\pi]$ by adding/subtracting 2π. This phase "wrapping" effect is undesirable and must be rectified prior

28

to further processing by the localization algorithm. The phase unwrapping algorithm performs this task.

Figure 2.7 is an example of the complexities of phase wrapping. Figure 2.7.a depicts the ideal, "unwrapped" phase variation across the X axis. As the phase value exceeds ±180° (see Figure 2.7.b), a noticeable jump in phase is evident as the phase is wrapped within the limits. This jump is detected by the phase unwrapping algorithm and is properly corrected.

The phase unwrapping algorithm compares the phase difference between two adjacent elements. If the difference exceeds ±π radians, the unwrapping algorithm is activated and a phase correction is made. The routine then moves to the next adjacent element and performs the same logic check and correction as necessary. Prior to discussing the details of the logic steps performed in the unwrap algorithm, we will first examine the basis for choosing ±π as the criteria for phase wrap detection. The maximum phase difference resulting from wave propagation (Θ_r) that could exist between adjacent elements is equal to π. If a phase difference exists that is greater than π, then it must be due to phase wrapping.

The two extreme cases that yield the maximum phase slope across the X axis are shown in Figure 2.8. The first example is a contact located in the extreme near-field at a broadside orientation to the array. An additional constraint is that the maximum slope only occurs at the highest harmonic. The second example is a target located at endfire relative to

29
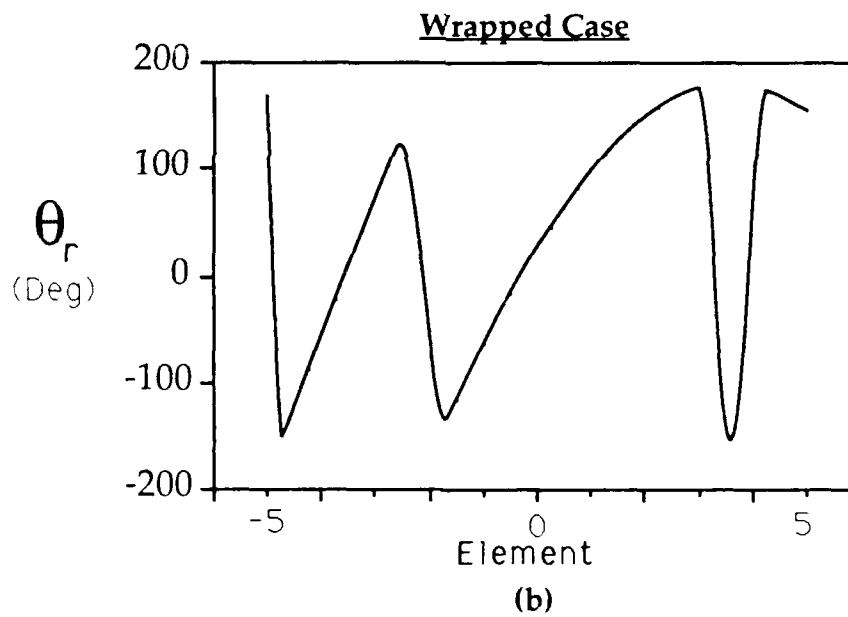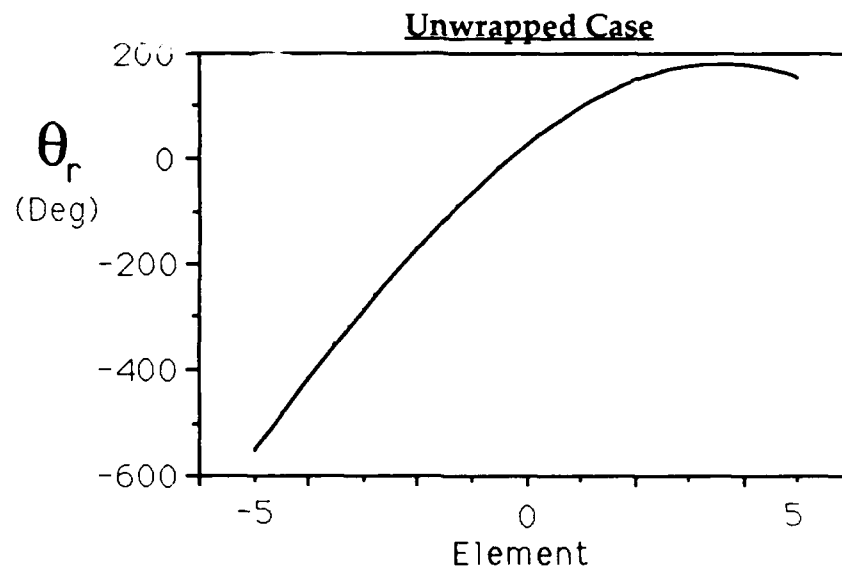
Figure 2.7   The Complexities of Phase Wrapping.

Unwrapped Phase across X axis
(Extreme Near Field, Broadside, q = Kmax)

(a)

Unwrapped Phase across X axis
(Endfire, Far Field, q = Kmax)

(b)
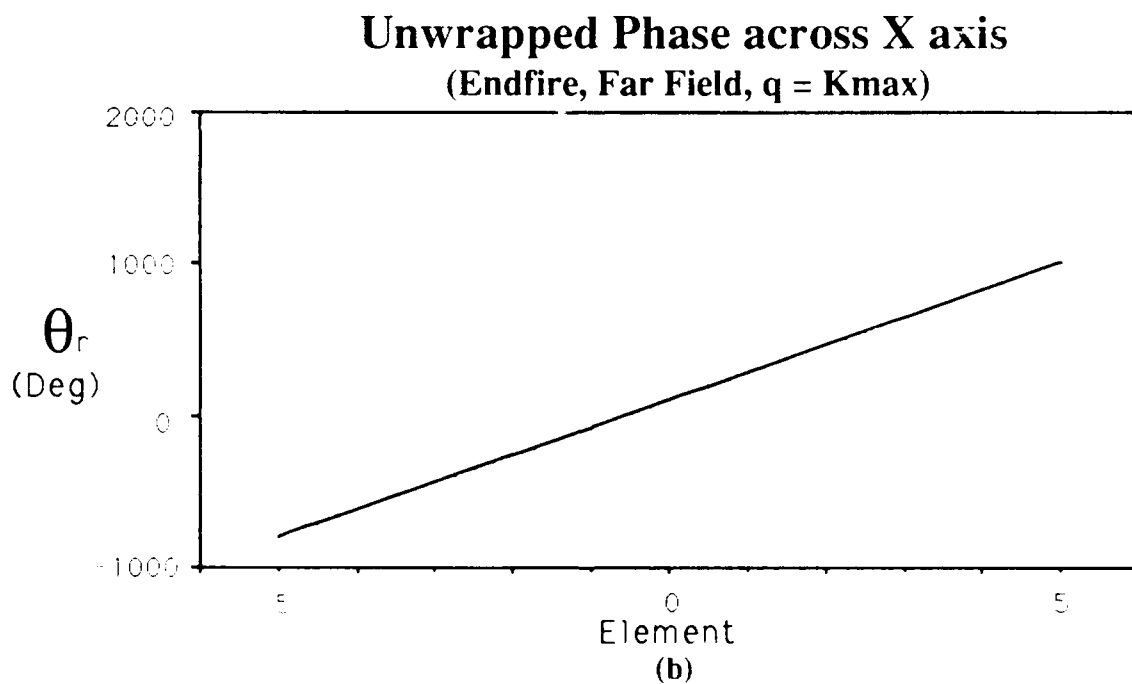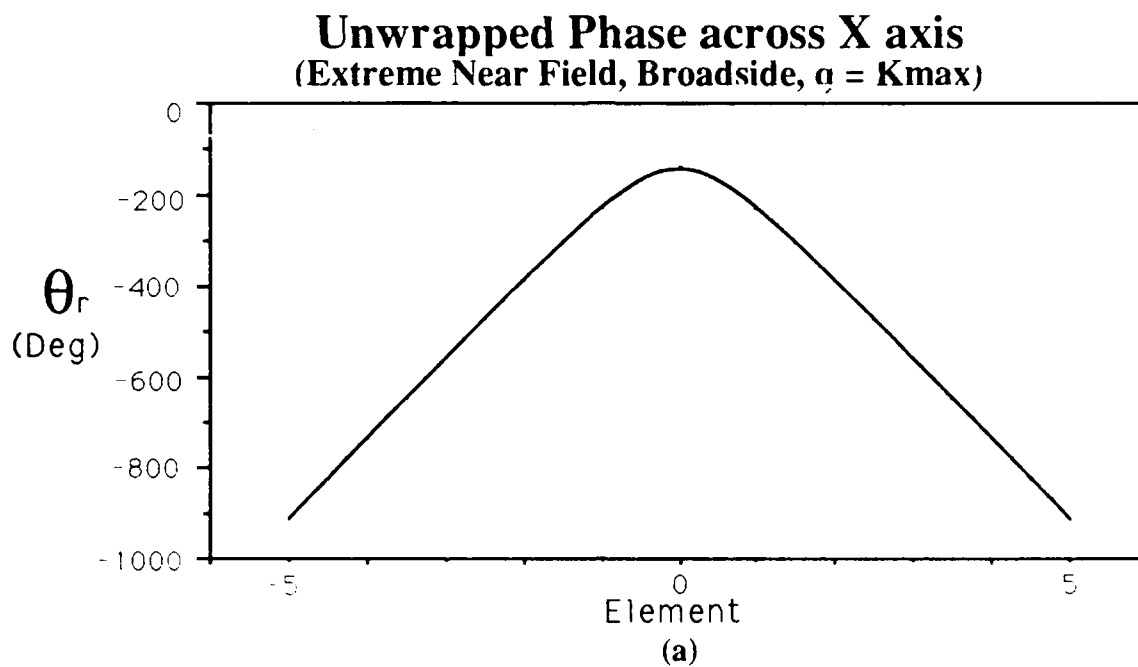
Figure 2.8   Cases Where the Phase Difference Between Elements
Approaches the Limiting Value of 180 Degrees.

31

the array and positioned in the far-field. The maximum slope for this case also occurs at the highest harmonic only. Starting with our expression for the radiated phase Θ_r (see Equation (2.27)), we will apply the conditions of these two extreme cases and calculate the maximum slope.

First, let us rewrite Equation (2.27) for use in this section:

$$\theta_r = -\frac{2\pi q f_0}{c}\left[r_0{}^2 - 2r_0\left(u_0 m d_x + v_0 n d_y\right) + \left(m d_x\right)^2 + \left(n d_y\right)^2\right]^{1/2} \qquad (2.47)$$

For each case we will only perform the analysis across the X axis, since similar results can be derived assuming the Y axis. Therefore, we set the index in the Y direction, n = 0. In the limiting near-field case, the target is located at broadside relative to the array. As a result, the direction cosine term u_o is equal to zero. For a target positioned in the very near field, the square of the range term r_o is considered negligible as compared to $(m d_x)^2$. Therefore, Equation (2.47) can be simplified as follows:

$$\theta_r = \pm\frac{2\pi K_{max} f_0\, m\, d_x}{c} \qquad (2.48)$$

where K_{max} is the highest harmonic. The derivative of Θ_r with respect to element number m is equal to

$$\left(\frac{d\theta_r}{dm}\right)_{max} = \pm\frac{2\pi K_{max} f_0\, d_x}{c}. \qquad (2.49)$$

32

By using Equation (2.34) through Equation (2.36), the interelement spacing term d_x can be expressed as

$$d_x = \frac{c}{2 K_{max} f_0}.$$

(2.50)

Substituting Equation (2.50) into Equation (2.49) yields

$$\left(\frac{d\theta_r}{dm}\right)_{max} = \pm \pi.$$

(2.51)

For the second case, the target is located at endfire. Therefore, the maximum value that u_o can attain is ± 1. If we set $u_o = \pm 1$, then Equation (2.47) simplifies to

$$\theta_r = -\frac{2\pi K_{max} f_0}{c}\left[r_0{}^2 - 2r_0(md_x) + (md_x)^2 \right]^{1/2}.$$

(2.52)

The term inside the radical of Equation (2.52) can be rewritten as

$$r_0{}^2 - 2r_0(md_x) + (md_x)^2 = (r_0 - md_x)^2.$$

(2.53)

Therefore, the radiated phase can be expressed as

$$\theta_r = \pm \frac{2\pi K_{max} f_0}{c}(r_0 - md_x).$$

(2.54)

Taking the derivative with respect to m yields

33

$$\left(\frac{d\theta_r}{dm}\right)_{max} = \pm \frac{2\pi\, K_{max}\, f_0\, d_x}{c}. \qquad (2.55)$$

Finally, substituting Equation (2.50) for d_x into Equation (2.55) yields the maximum slope

$$\left(\frac{d\theta_r}{dm}\right)_{max} = \pm \pi. \qquad (2.56)$$

The phase unwrapping algorithm uses this value of π as the criterion for detecting a phase wrap between elements. The logic flow of the phase unwrapping algorithm is pictured in Figure 2.9. The phase unwrapping algorithm begins at the center element of the array. If the unwrapping is to be performed in the (+) X direction, then the step size is set equal to unity (for negative X direction, $s = -1$). Two iterations through the comparator section of the routine are required. This double pass approach is necessary due to the effects of wavefront curvature. That is to say, since the slope of the phase variation can be both positive and negative across the axis, the direction of unwrapping becomes more complex. In the first pass, the phase values between adjacent elements are compared. When a wrap is detected a positive correction is applied to the phase value. This positive correction is equal to $+2k\pi$, where the constant k is the number of times the phase value at the adjacent element has been wrapped. On the second pass through this routine, a

34
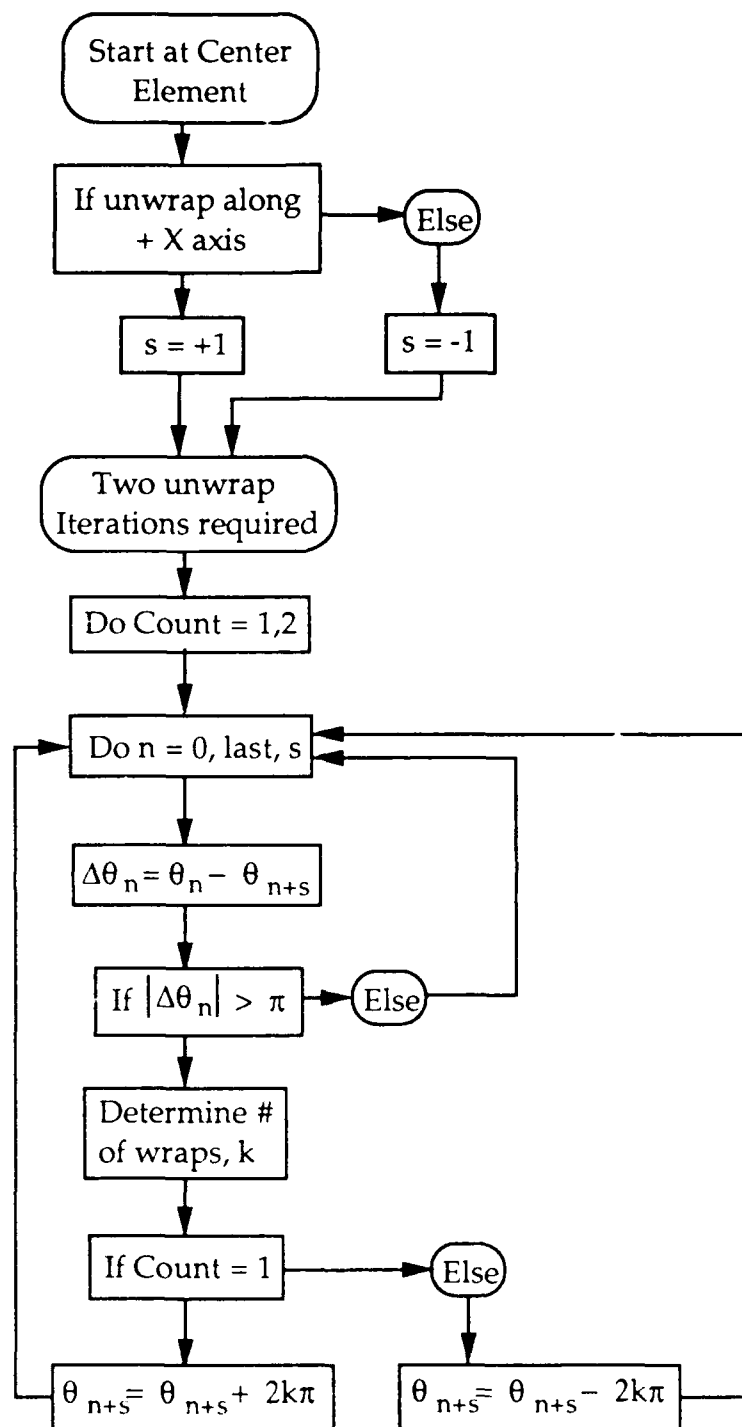
Figure 2.9   Logic Flow of the Unwrapping Algorithm.

backup check of the phase unwrapping is conducted. If the phase value has been incorrectly unwrapped, the algorithm applies a negative correction. In this way, even in cases of significant wavefront curvature, the values are correctly unwrapped between the elements.

This process is repeated along the (+) X axis out to the final element. The routine then returns to the center element and iterates along the (-) X axis. Upon unwrapping the X axis, the algorithm operates on the Y axis in a similar manner. Since the center element is a common element for both axes, it is essential to start the unwrapping here for both cases (versus beginning at the end of either axis). The output from this section is a set of unwrapped, steady-state, phase weights at the elements along the X and Y axes. The final step in the signal processing routine is to smooth the phase values along the X and Y axes using non-linear least-squares estimation.

5. **Non-Linear Least-Squares Estimation**

The two major sources of phase distortion, that is, Θ_n and Θ_{wrap}, have been eliminated using the techniques mentioned in the last two sections. One further step is necessary prior to passing the unwrapped, steady-state phase information to the localization algorithm. Although the modified LMS adaptive algorithms cancel the majority of the noise corruption in the received signals, some jitter still exists in the steady-state phases. The localization algorithm

36

uses the phase information at three elements along the X and Y axes to estimate the range to the target. Specifically, the phase values at the end elements and the center element are used. Our research has shown that the slight jitter that may exist in the phase values at these elements can have a radical impact on the resulting range estimate. Therefore, the last step in our signal processing routine is to find a curve that represents the best fit given the discrete phase values along the two axes. The technique used to perform this smoothing is non-linear least-squares estimation.

Given n+1 equally spaced data points assigned to values of x, where x = 0, 1, . . . , n, a non-linear curve that best fits this data can be determined using orthogonal polynomials [Ref. 7]. The equation of this curve is given by [Ref. 7]

$$P(x) = a_0 P_{n0}(x) + a_1 P_{n1}(x) + \cdots + a_m P_{nm}(x) \qquad (2.57)$$

where m is the degree of the polynomial, $P_{no}(x)$, $P_{n1}(x)$, ..., $P_{nm}(x)$ are the orthogonal polynomials, and a_o, a_1, ..., a_m are the coefficients of the orthogonal polynomials. Orthogonal polynomials have the following property:

$$\sum_{x=0}^{n} P_{nj}(x) P_{nk}(x) = 0, \quad j \neq k . \qquad (2.58)$$

The general formula used in computing the orthogonal polynomials is [Ref. 7]

$$P_{nm}(x) = \sum_{i=0}^{m} (-1)^i \binom{m}{i}\binom{m+1}{i} \frac{(x)^i}{(n)^i}, \quad m = 0, 1, 2, \ldots, n \tag{2.59}$$

where
$$\binom{m}{i} = \frac{m!}{(m+1)!\; i!}. \tag{2.60}$$

Using this formula, the first four polynomials are given as follows:

$$P_{n0}(x) = 1, \tag{2.61}$$

$$P_{n1}(x) = 1 - 2\frac{x}{n}, \tag{2.62}$$

$$P_{n2}(x) = 1 - 6\frac{x}{n} + 6\frac{x(x-1)}{n(n-1)}, \tag{2.63}$$

and
$$P_{n3}(x) = 1 - 12\frac{x}{n} + 30\frac{x(x-1)}{n(n-1)} - 20\frac{x(x-1)(x-2)}{n(n-1)(n-2)}. \tag{2.64}$$

By using these four polynomials and by calculating the values for their respective coefficients, we can construct a cubic polynomial to fit the given phase data while minimizing the least-squares error. The equation for calculating the coefficients is given by [Ref. 7]

$$a_i = \frac{\displaystyle\sum_{x=0}^{n} f(x)\, P_{ni}(x)}{\displaystyle\sum_{x=0}^{n} P_{ni}^2(x)}. \quad i = 0, 1, \ldots, m, \tag{2.65}$$

38

where the values of f(x) are the phase values given for each element along a particular axis.

Using orthogonal polynomials, one can derive the equation for a curve of degree m with minimum least-squares error, where $m \leq n$ (n+1 is the number of data points). For the results that we will present in Chapter III, we performed a best fit approximation using a cubic polynomial (m = 3). A polynomial of this degree was adequate to perform the smoothing required for our phase data.

One additional value that we calculated and monitored in our computer runs was the actual least-squares error. This error can be calculated from the following equation [Ref. 7]:

$$E = \sum_{x=0}^{n} f^2(x) - \sum_{i=0}^{m}\left[a_i^2 \sum_{x=0}^{n} P_{ni}^2(x) \right].$$
(2.66)

The value of this error gives an indication of how well the non-linear curve fits the data.

This concludes all the steps used in the frequency-domain signal processing section of our research. The output from this section is a set of smoothed phase values for the elements along the X and Y axes where the effects of noise have been minimized and the frequency-domain signal has been smoothed, and unwrapped. The target localization algorithm will take these values and determine an estimation of the spherical location of the target.

C.   TARGET LOCALIZATION IN SPHERICAL COORDINATES

Beginning with the noise-corrupted output electrical signals at the elements in the receive array, our goal has been to take this time-domain information and localize a target or a group of targets in spherical coordinates. One intermediary step was to convert the signals into the frequency domain and filter out as much of the distortion due to noise as possible. With this accomplished, we are now in a position to take these processed signals and work backwards in order localize the targets.

The localization algorithm applies the physical properties of wave propagation developed in Section II.A, and utilizes the symmetry of the receive array to obtain a position estimate. The first step in this routine is to isolate the terms that contribute to wavefront curvature, and then to estimate the target range. Having solved for this parameter, the wavefront curvature is cancelled, leaving a linear phase relationship. By manipulating the slope information from this conditioned phase data, the angular position of the target is determined (see Figure 2.10).

1.   Three Point Range Algorithm

Our first step in the localization problem is to manipulate the unwrapped, smoothed, steady-state phase information received from the signal processing routine to estimate target range. We denote this processed phase as Θ_p.

40
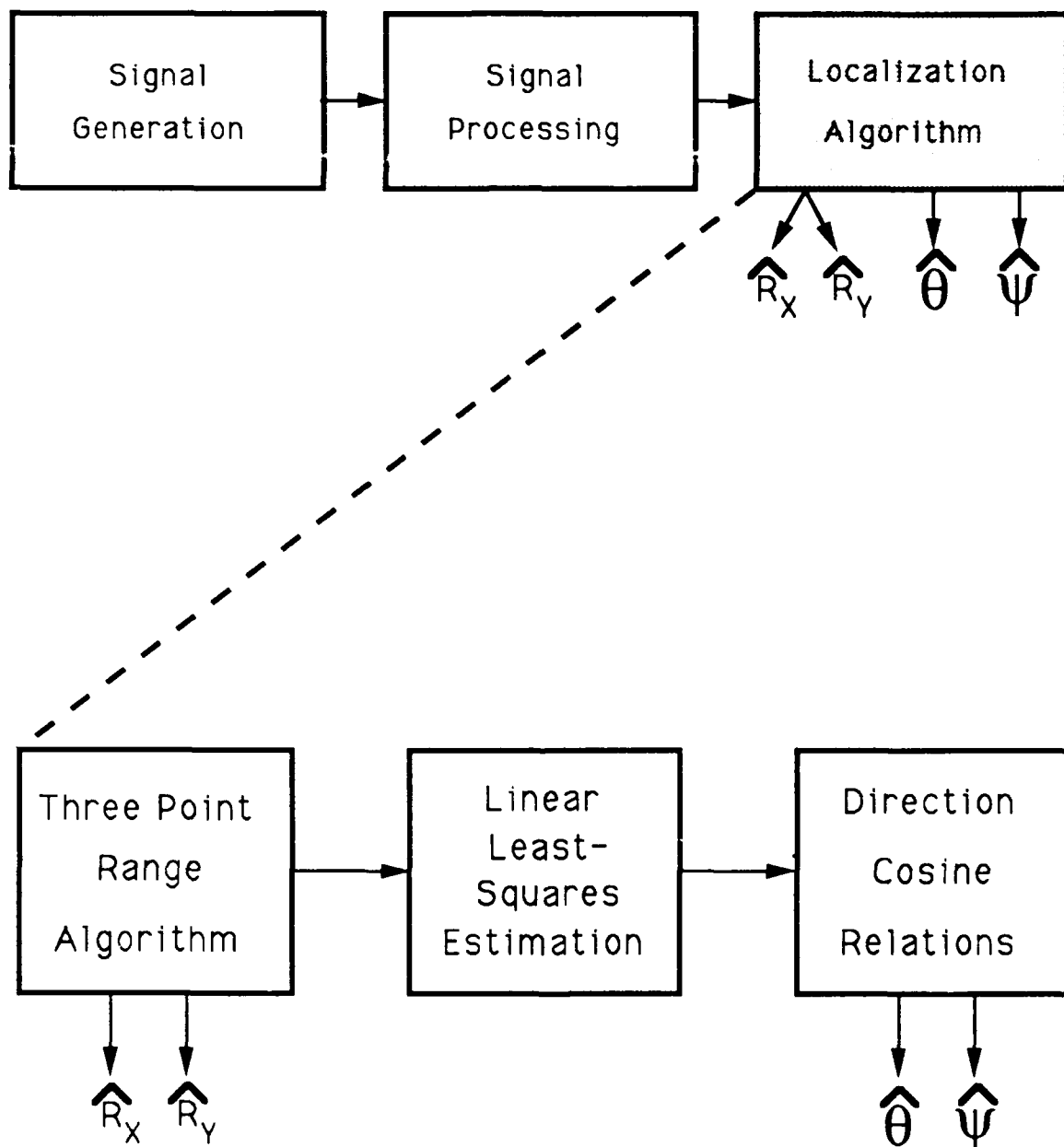
**Figure 2.10   Block Diagram Representation of the Major Steps
Performed in the Localization Algorithm.**

41

As discussed in section II.B.1, θ_p is comprised of three phase components, that is,

$$\theta_p = \theta_r + \theta_q + \theta_c \qquad (2.67)$$

where θ_r is the phase due to wave propagation, θ_q is the phase of the Fourier series coefficient c_q, and θ_c is the phase term that represents a constant phase shift that is generated at each element due to the LMS algorithm. In our range algorithm, θ_q and θ_c are grouped together and considered as one constant phase term $\theta_{q'}$, that is,

$$\theta_{q'} = \theta_q + \theta_c. \qquad (2.68)$$

Recall from Equation (2.27) that, the radiated phase is given by

$$\theta_r(q,m,n) = -\frac{2\pi q f_0}{c}\left[r_0^2 - 2r_0\left(u_0 m d_x + v_0 n d_y\right) + \left(m d_x\right)^2 + \left(n d_y\right)^2\right]^{1/2}. \qquad (2.69)$$

The range algorithm uses the phase information at three elements per X and Y axis to estimate range. For this analysis, let us consider the X axis (set n=0). The phase of the two end elements on each side of the X axis are combined to form one equation in terms of range r_0 and $\theta_{q'}$. Since the end elements are symmetrical about the center element, this equation can be simplified. The second equation is formed by the value of the phase at the center element. This equation

42

is also a function of our two unknowns, r_o and $\theta_{q'}$. These two equations are manipulated to solve for the two unknowns. In this fashion, we obtain a value for the range based on three elements along the X axis. The same approach is implemented on the three corresponding elements on the Y axis. As a result, we obtain two estimates of the range.

The processed phase at the center element is obtained by combining Equation (2.67) through Equation (2.69) and setting m=0 and n=0:

$$\theta_p(q,0,0) = \theta_{q'} - \frac{2\pi q f_0}{c} r_0. \tag{2.70}$$

This is the first equation needed to solve for our two unknowns. The equation from the symmetrical end elements requires a more detailed derivation. First, from Equation (2.67) and Equation (2.68), we can write that

$$\theta_p(q,m,n) - \theta_{q'} = \theta_r(q,m,n). \tag{2.71}$$

Assuming M_{total} elements along the X axis, the element number m of these two symmetrical elements can be expressed as $\pm m'$, where m' is defined as

$$m' \equiv (M_{total} - 1)/2. \tag{2.72}$$

43

Let us derive an equation at element -m' first. To eliminate the radical of Equation (2.69), we square both sides of Equation (2.71) after substituting Equation (2.69) into Equation (2.71). The element number -m' is then substituted in place of m yielding

$$\theta_p^2{}_{(q,-m',0)} - 2\upsilon_p{}_{(q,-m',0)}\theta_{q'} + \theta_{q'}^2 = \frac{4\pi^2 q^2 f_0^2}{c^2}\left[r_0^2 - 2r_0 u_0(-m')d_x + (-m'd_x)^2\right]. \qquad (2.73)$$

In the same manner, the equation at +m' is given by

$$\theta_p^2{}_{(q,m',0)} - 2\theta_p{}_{(q,m',0)}\theta_{q'} + \theta_{q'}^2 = \frac{4\pi^2 q^2 f_0^2}{c^2}\left[r_0^2 - 2r_0 u_0 m'd_x + (m'd_x)^2\right]. \qquad (2.74)$$

Equation (2.73) is added to Equation (2.74) to cancel out the term containing the direction cosine information to yield

$$\theta_p^2{}_{(q,-m',0)} + \theta_p^2{}_{(q,m',0)} - 2\theta_q\left[\theta_p{}_{(q,-m',0)} + \theta_p{}_{(q,m',0)}\right] + 2\theta_{q'}^2 = \frac{8\pi^2 q^2 f_0^2}{c^2}\left[r_0^2 + (m'd_x)^2\right]. \qquad (2.75)$$

This is the second equation needed to solve for our two unknowns. Next, we square both sides of Equation (2.70) to form

$$\theta_p^2{}_{(q,0,0)} - 2\theta_p{}_{(q,0,0)}\theta_{q'} + \theta_{q'}^2 = \frac{4\pi^2 q^2 f_0^2}{c^2} r_0^2. \qquad (2.76)$$

This equation is then substituted into Equation (2.75) to solve for the $\theta_{q'}$ estimate,

44

$$\hat{\theta}_{q'} = \frac{\left[2\theta_{p_0}^2 - \theta_{p_{-m'}}^2 - \theta_{p_{m'}}^2 + \dfrac{8\pi^2 q^2 f_0^2}{c^2}(m' d_x)^2\right]}{2\left[2\theta_{p_0} - \left(\theta_{p_{-m'}} + \theta_{p_{m'}}\right)\right]} , \qquad (2.77)$$

which is one of the two unknowns. Having solved for the first unknown, we substitute the estimated value for $\theta_{q'}$ into Equation (2.70) to solve for r_0. Upon algebraically solving for r_0 in terms of $\theta_{q'}$ from Equation (2.70), we obtain

$$\hat{r}_0 = \left[\theta_{q'} - \theta_p(q,0,0)\right]\left(\frac{c}{2\pi q f_0}\right). \qquad (2.78)$$

In summary, we cancelled the term that contains the direction cosine variable u_0 in Equation (2.69) by using symmetrical elements along the X axis ($\pm m'$). We combined the resulting equations derived from these two elements with the equation representing the phase at the center element. From these three elements, we formed two equations to solve for two unknowns. One of these unknowns is the range estimate to the target, $\hat{r}_0$. The routine is then repeated for the corresponding three elements along the Y axis.

2. Estimation of Bearing and Depression Angles

Knowing the range estimate $\hat{r}_0$ and the value for $\theta_{q'}$ greatly simplifies the task of solving for the angular estimates. We manipulate the terms containing these two quantities within the phase at each element and effectively cancel out the wavefront curvature along the X and Y axes. We perform a linear least-squares estimation to calculate a

line that best fits this corrected phase data. The slope of this line is equal to the direction cosine u_0 given data along the X axis; v_0 for Y axis data. From the direction cosine estimates, we can calculate the bearing and depression angles.

For this angular analysis, our goal is to formulate a new phase term that is a function of a single direction cosine only. Specifically, we solve for the term $u_0 m$ by setting $n=0$ in Equation (2.69) and define this value as our new phase term. The first step is to subtract the estimated value of θ_q, found in the previous section from the phase value at each element, to solve for θ_r (see Equation 2.71). We substitute this value for θ_r into Equation (2.69) and solve for $u_0 m$ as follows

$$\theta_{u_0}(q,m,n) = u_0 m = \frac{\left[\frac{c}{2\pi q f_0}\theta_r(q,m,n)\right]^2 - \hat{r}_0^{\,2} - (m\,d_x)^2}{-2\hat{r}_0\,d_x}, \quad n = 0. \quad (2.79)$$

By setting $m=0$ and performing a similar algebraic manipulation, $v_0 n$ can be solved for as

$$\theta_{v_0}(q,m,n) = v_0 n = \frac{\left[\frac{c}{2\pi q f_0}\theta_r(q,m,n)\right]^2 - \hat{r}_0^{\,2} - (n\,d_y)^2}{-2\hat{r}_0\,d_y}, \quad m = 0. \quad (2.80)$$

Using these two equations, we recalculate the new phase at each element along the X and Y axes. These conditioned phases are linear along the X and Y axes. From the non-linear estimation discussion of Section II.B.5, we utilize the first two orthogonal polynomials P_{n0} and P_{n1} (see Equation (2.61) and

Equation (2.62)) to perform a linear least-squares estimation on this data. The slope of the resulting line estimates is equal to u_o and v_o, respectively.

From these calculated values of u_o and v_o, we can calculate the estimates of the bearing and depression angles as follows:

$$\widehat{\theta}_0 = \sin^{-1}\left[\left(u_0^2 + v_0^2\right)^{1/2}\right] \qquad (2.81)$$

and

$$\widehat{\psi}_0 = \tan^{-1}\left(\frac{v_0}{u_0}\right). \qquad (2.82)$$

With this information, our localization of the target is complete (see Figure 2.3).

47

III. SIMULATION RESULTS

Three major categories were chosen in order to validate
the significant capabilities of the localization algorithm.
In Section III.A, the results validating the full angular
coverage capability are presented. Full angular coverage
implies that the target can be localized regardless of its
relative position to the receive array. The multi-harmonic
capability of the algorithm is exercised in Section III.B.
The two test cases presented review the performance of the
algorithm given a single target with several harmonics,
covering a wide frequency spectrum. In the final section of
this chapter, Section III.C, we examine the multiple broadband
target performance of the algorithm. Three targets with two
unique harmonics each and at different locations are tested.

Prior to presenting the results from these test cases, a
review of the design limitations of our computer simulation
is necessary. The computer code is written in the Fortran
language and is organized in modular sections (i.e.,
subroutines reflect major analysis blocks in Figures 2.4 and
2.9). Since the program was written as a research tool, the
emphasis was placed on making the code detailed and easy to
follow. One adverse consequence of this decision is longer
processing times. Given the restrictions on computer

simulation run times, certain self-imposed design limitations were required.

The first design limitation is the number of time samples taken when converting the signal to the frequency domain. In all of the test cases conducted, 65 time samples at each element were taken. In the context of our research, we found that our localization estimates improved when we took more time-domain samples over the data record. This principle is also formally documented in [Ref. 1]. The other major constraint was the number of elements that comprised the planar array. In each of the following test cases, we used an 11 × 11 element array. Two beneficial results occur as we increase the number of elements in the receive array. First, the dimensions of the array increase. With a larger array, the wavefront curvature becomes more pronounced. Secondly, the performance of the modified, frequency-domain, LMS adaptive algorithm, as well as the curve fitting accomplished by the non-linear least-squares estimation routine are enhanced as the data from more elements is processed.

In each of the test cases, the simulation run was first conducted in a noise-free environment to validate the propagation and localization models. Once the baseline results were generated, the test cases were repeated in a noise environment. The two noise environments chosen represented SNR values of 0.0 dB and -3.0 dB. An overview of the algorithm's performance is presented at the beginning of

49

the respective test case. The average estimation error of the target's location at a given harmonic are presented for each test case.

The modified, frequency-domain LMS adaptive algorithms conduct a specified number of iterations as the complex weights are recursively updated (see Section II.B.3). In all of the noise cases that were tested, the number of iterations used in the LMS adaptive algorithms was equal to 100. The estimation errors that are presented for each test case are average values. For a given SNR, the average estimation errors for the range, bearing and depression angles were obtained by running the computer simulation 50 times.

Lastly, since the range estimate is very sensitive to wavefront curvature, a plot of the ideal phase variation across the X or Y axis is given for each test case. Aside from the actual range position (i.e., NF/FF), other factors that affect wavefront curvature include frequency (i.e., harmonic number) and relative geometry. Rather than examine the contribution of each of these individual effects, the performance of the range estimate will be considered in light of the plot of wavefront curvature for a given target (location) and harmonic number.

A. CATEGORY I: VALIDATION OF THE "FULL ANGULAR COVERAGE" CAPABILITY

A single target was placed at three positions relative to the center of the receive array. The first geometry analyzed is with the target located at a position broadside relative to the receive array. The range of the target is then varied to examine the range limitations of the algorithm. In the second test case, an arbitrary position between broadside and endfire geometries is analyzed. For these two cases, a single frequency component of 1000 Hz was used in analyzing the target. In the final case, the target is placed at a position endfire to the plane of the array. Three harmonics with a fundamental frequency of 1000 Hz were used for the target in this case.

1. Case I.A: Target Located Broadside Relative to the Planar Array

In this case, the target is located at a depression angle Θ_c of 0.0' (i.e., broadside relative to the array). In Table 1, the no-noise data is presented. Three range cases are summarized in this table. At a range of 5.89 meters, the target is located well within the near-field $(0.1*\rho)$. A second range located at a position in the middle of the NF region, 29.4 meters $(0.5*\rho)$ was tested. The third range examined represents a position in the extreme far-field, 58.9 km $(1000*\rho)$ and was chosen to show how well the algorithm works in this ideal no-noise case, given minimal wavefront

51

TABLE 1

CASE I.A.1- TARGET AT BROADSIDE, SINGLE HARMONIC, NO NOISE.

LMS Case	Actual Location			Average Estimation Error				Range % Diff	
	R_0 (m)	θ_0 (deg)	ψ_0 (deg)	$e_{R_{0x}}$ (m)	$e_{R_{0y}}$ (m)	e_{θ_0} (deg)	e_{ψ_0} (deg)	$e_{R_{0x}}$	$e_{R_{0y}}$
	$\underline{0.1*\rho}$								
Flat	5.8905	0.0	0.0	-0.414	-0.414	0.0	-18.3	-7.0	-7.0
Curve	5.8905	0.0	0.0	-0.002	-0.002	0.0	-45.0	0.0	0.0
	$\underline{0.5*\rho}$								
Flat	29.452	0.0	0.0	-0.095	-0.095	0.0	-90.0	-0.3	-0.3
Curve	29.452	0.0	0.0	0.002	0.002	0.0	-45.0	0.0	0.0
	$\underline{1000*\rho}$								
Flat	58905	0.0	0.0	-0.006	-0.006	0.0	-11.3	0.0	0.0
Curve	58905	0.0	0.0	-0.004	-0.004	0.0	-45.0	0.0	0.0

curvature. The plot of the wavefront curvature for these three range values is given in Figure 3.1.

The results from the two modified LMS adaptive algorithms are presented in Table 1. The algorithm that assumes separable weights, LMS_{flat}, is identified as "Flat" in the table. The algorithm assuming non-separable phase weights, LMS_{curve}, is denoted by "Curve". Recall that LMS_{flat} is ideally suited for minimal wavefront curvature. This property is supported by the results in that, as target range increases, the range estimation error decreases. In fact, when the target is located in the extreme NF region, the range estimate using LMS_{flat} is 7% larger than the actual range value. LMS_{curve} performs well at all three of these range cases.

Note the wavefront curvature in Figure 3.1 for the FF case $(1000*\rho)$. For this no-noise case, both algorithms accurately estimated this extreme range value. For all the results presented, both algorithms correctly estimated the depres:ion angle Θ_o. In this case, the bearing angle is arbitrary. Throughout the remaining examples, we will only discuss the highlights of the results. Since both algorithms generally give good estimates of the angular information, most of our discussion will be focused on range estimates.

Table 2 summarizes the broadside results for the 0.0 dB SNR case. The LMS_{curve} algorithm does well in the near field. However, as the range position is increased to a value

53

Figure 3.1 Phase Variation Across the X-axis as a Function of Range for Case IA1.

TABLE 2

CASE I.A.2- TARGET AT BROADSIDE, SINGLE HARMONIC, 0.0 DB.

LMS Case	Actual Location			Average Estimation Error				Range % Diff	
	R_0 (m)	θ_0 (deg)	ψ_0 (deg)	$e_{R_{0x}}$ (m)	$e_{R_{0y}}$ (m)	e_{θ_0} (deg)	e_{ψ_0} (deg)	$e_{R_{0x}}$	$e_{R_{0y}}$
	$\underline{0.1*\rho}$								
Flat	5.8905	0.0	0.0	-0.409	-0.423	-0.1	-174.6	-6.9	-7.2
Curve	5.8905	0.0	0.0	0.002	-0.033	-0.3	-166.2	0.0	0.0
	$\underline{0.5*\rho}$								
Flat	29.452	0.0	0.0	-0.150	-0.449	-0.1	-168.9	-0.5	-1.5
Curve	29.452	0.0	0.0	-0.713	-0.635	-0.3	-172.8	-2.4	-3.1
	$\underline{1.0*\rho}$								
Flat	58.905	0.0	0.0	-0.295	0.770	-0.1	-167.2	-0.5	1.3
Curve	58.905	0.0	0.0	-1.701	-1.852	-0.3	-164.8	-2.9	-3.1
	$\underline{3.0*\rho}$								
Flat	176.72	0.0	0.0	-3.52	-16.42	-0.1	-163.0	-2.0	-9.3
Curve	176.72	0.0	0.0	-79.2	-164.1	-0.3	-180.7	-44.8	-92.3
	$\underline{4.0*\rho}$								
Flat	235.6	0.0	0.0	-20.4	-12.9	-0.1	-185.0	-8.7	-5.5
Curve	235.6	0.0	0.0	-161.8	-711.4	-0.2	-192.9	-68.7	-302
	$\underline{5.0*\rho}$								
Flat	294.5	0.0	0.0	-117.2	-28.1	-0.1	-176.6	-39.8	-9.5
Curve	294.5	0.0	0.0	294.6	60.8	-0.1	-182.3	100	20.6

into the FF, the range estimates become unreliable (i.e., range estimation error is large; X and Y estimates differ) due to minimal wavefront curvature. LMS_{flat} estimates range out to a position of $3*\rho$ adequately. Figure 3.2 shows the difference in wavefront curvature for $3*\rho$ to $5*\rho$, the region where the range estimates of the LMS_{flat} algorithm become erroneous. In the remainder of our test cases, the range estimates of LMS_{flat} will be shown as superior to those of LMS_{curve} as we enter the FF region. However, LMS_{curve} will be seen to perform better in the extreme NF. This property reflects the assumptions made concerning the complex phase weights (i.e., separable versus non-separable). Even as range estimates became unsatisfactory, both algorithms continued to estimate the angular information to within a few tenths of a degree.

Table 3 summarizes the broadside results for -3.0 dB SNR. As expected, in this noisier environment, the estimates of both algorithms are degraded. Once again, since range is the most sensitive of the estimated spherical coordinates, the corresponding estimates are more severely degraded. Note that the Θ_0 estimate is still accurate even as the range estimate becomes more unreliable.

2. **Case I.B: Target with Arbitrary Position**

For this test case, the target is positioned at an arbitrary position given a bearing angle Ψ_0 of 140° and a depression angle Θ_0 of 35°. Figure 3.3 depicts the wavefront curvature for the range values tested in this case. At this
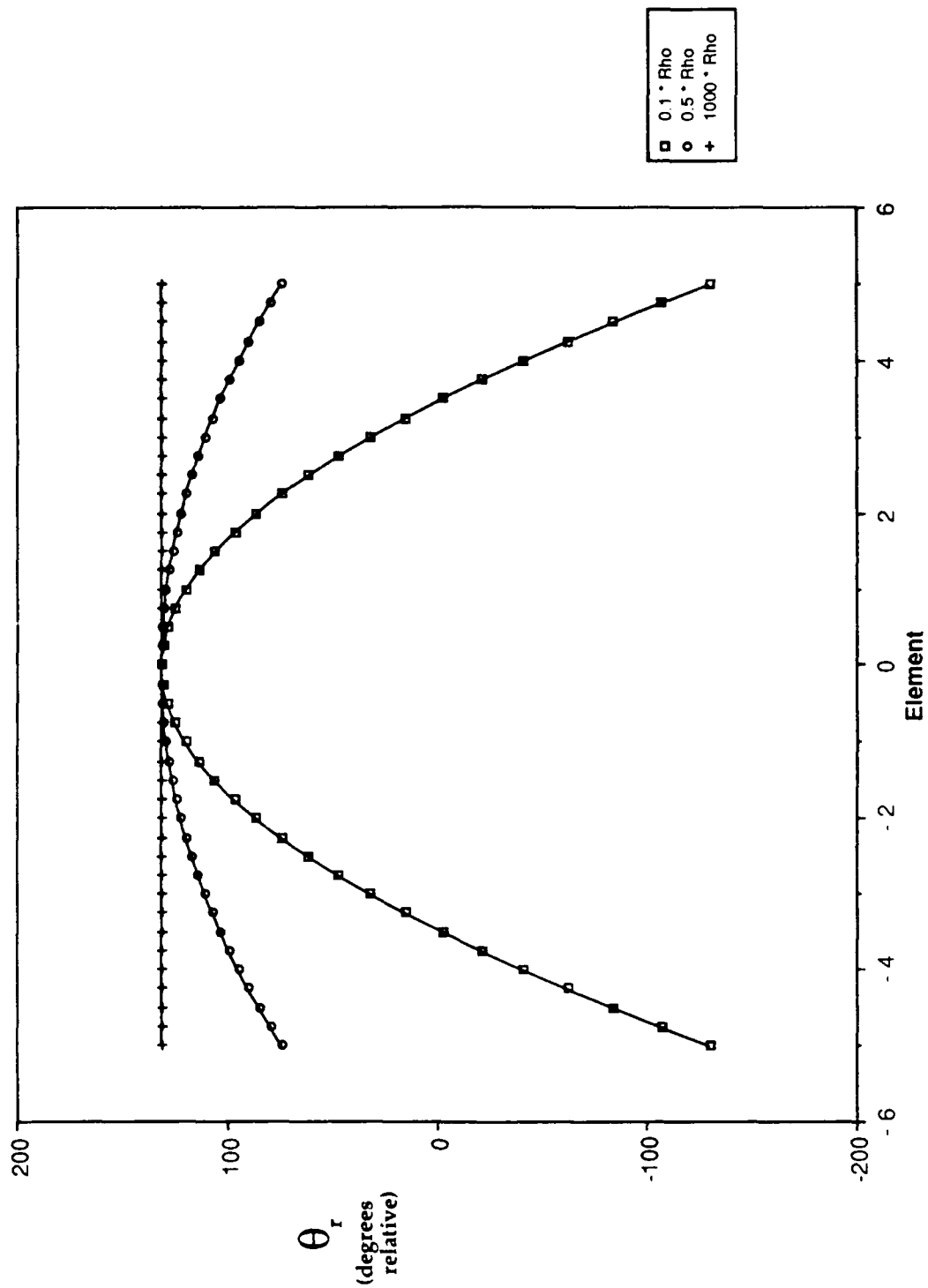
56
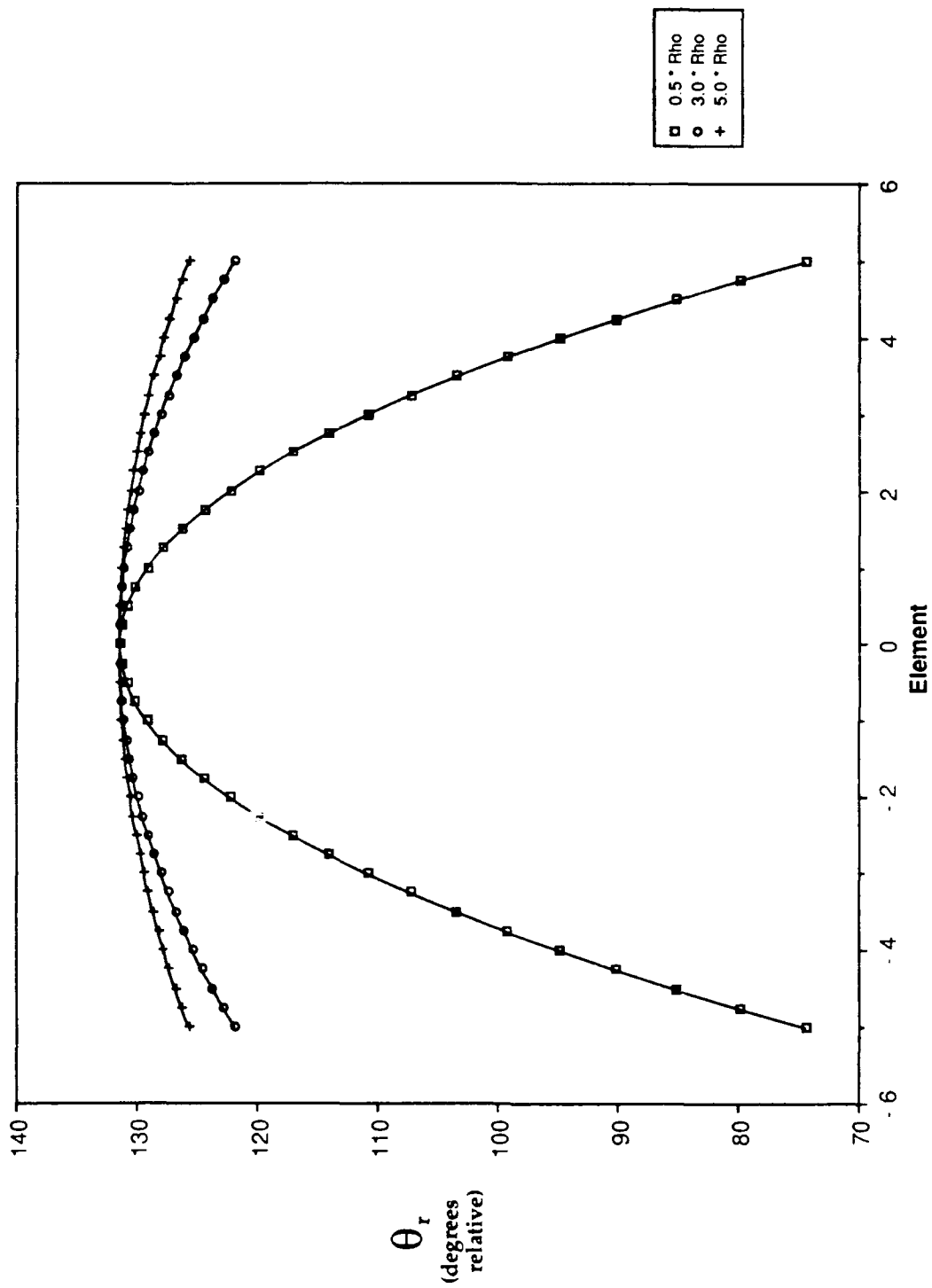
Figure 3.2 Phase Variation Across the X-axis as a Function of Range for Case IA2, IA3.

TABLE 3

CASE I.A.3- TARGET AT BROADSIDE, SINGLE HARMONIC, -3.0 DB.

LMS Case	Actual Location			Average Estimation Error				Range % Diff	
	R_0 (m)	θ_0 (deg)	ψ_0 (deg)	$e_{R_{0x}}$ (m)	$e_{R_{0y}}$ (m)	e_{θ_0} (deg)	e_{ψ_0} (deg)	$e_{R_{0x}}$	$e_{R_{0y}}$
	$\underline{0.1*\rho}$								
Flat	5.8905	0.0	0.0	-0.407	-0.428	-0.1	-175.1	-6.9	-7.3
Curve	5.8905	0.0	0.0	0.002	-0.049	-0.5	-167.2	0.0	-0.8
	$\underline{0.5*\rho}$								
Flat	29.452	0.0	0.0	-0.190	-0.606	-0.1	-168.5	-0.6	-2.1
Curve	29.452	0.0	0.0	-1.287	-1.129	-0.4	-172.0	-4.4	-3.8
	$\underline{1.0*\rho}$								
Flat	58.905	0.0	0.0	-0.518	0.960	-0.1	-174.7	-0.9	1.6
Curve	58.905	0.0	0.0	-3.789	-6.658	-0.4	-164.0	-6.4	-11.3
	$\underline{3.0*\rho}$								
Flat	176.72	0.0	0.0	-8.505	-31.53	-0.1	-162.8	-4.8	-17.8
Curve	176.72	0.0	0.0	338.9	203.8	-0.4	-187.5	-192	-115
	$\underline{4.0*\rho}$								
Flat	235.6	0.0	0.0	-58.5	-29.0	-0.1	-184.9	-24.8	-12.3
Curve	235.6	0.0	0.0	-48.7	36.0	-0.3	-193.2	-20.7	15.3
	$\underline{5.0*\rho}$								
Flat	294.5	0.0	0.0	-33.9	13.0	-0.1	-176.5	-11.5	4.4
Curve	294.5	0.0	0.0	227.0	-1534	-0.4	-174.8	77.1	-520
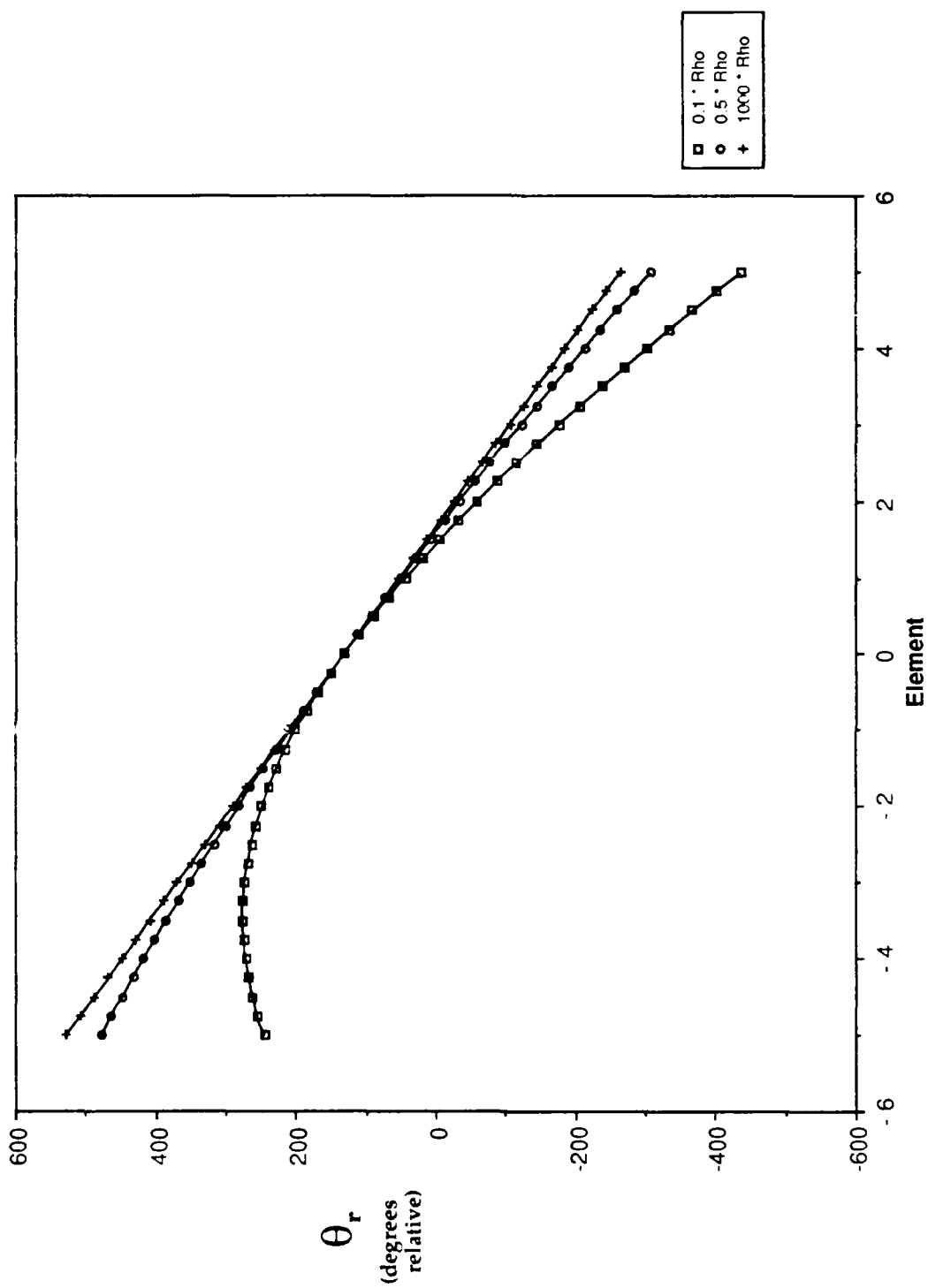
Figure 3.3 Phase Variation Across the X-axis as a Function of Range for Case IB.

geometry, the wavefront curvature is considerably less than the broadside case. The resulting range estimates in a noise environment bear witness to this fact.

Table 4 documents the results of the no-noise case. The results indicate minimal error even at a range of $1000*\rho$. Tables 5 and 6 summarize the performance of the two algorithms in a noise environment. The same trends that were discussed in the last section are evident. Once again, LMS_{flat} gives the most reliable maximum range (about $3*\rho$). The angular estimates are excellent in both noise environments.

3. Case I.C: Target with Endfire Geometry

This test case is significant in that it exposes two limitations in the target localization problem. One limitation occurs in the phase unwrapping routine performed in the signal processing section. The second deficiency observed in this test case can be traced to the range estimation equation in the localization algorithm. Specifically, at this extreme endfire position, the estimates of the localization algorithm become unreliable.

The first discrepancy occurs when analyzing the highest harmonic of a target located at an endfire position relative to the X or Y axis. From our discussion in Section II.B.4, we identified this extreme case as the basis for choosing π radians as the setpoint for the phase unwrapping algorithm. In our research, we observed that with noise corruption, or with the slight distortion that resulted from

60

TABLE 4

CASE I.B.1- TARGET AT ARBITRARY POSITION, SINGLE HARMONIC, NO NOISE.

LMS Case	Actual Location			Average Estimation Error				Range % Diff	
	R_0 (m)	θ_0 (deg)	ψ_0 (deg)	$e_{R_{0x}}$ (m)	$e_{R_{0y}}$ (m)	e_{θ_0} (deg)	e_{ψ_0} (deg)	$e_{R_{0x}}$	$e_{R_{0y}}$
	$0.1*\rho$								
Flat	5.8905	35.0	140.0	-0.198	-0.120	1.09	0.35	-3.4	-2.0
Curve	5.8905	35.0	140.0	-0.003	-0.002	0.01	-0.01	0.0	0.0
	$0.5*\rho$								
Flat	29.452	35.0	140.0	-0.071	-0.042	0.03	0.02	-0.2	-0.1
Curve	29.452	35.0	140.0	-0.002	-0.002	0.0	0.0	0.0	0.0
	$1000*\rho$								
Flat	58905	35.0	140.0	20.7	0.114	0.0	0.0	0.4	0.0
Curve	58905	35.0	140.0	24.4	21.7	0.0	0.0	0.4	0.4

TABLE 5

CASE I.B.2- TARGET AT ARBITRARY POSITION, SINGLE HARMONIC, 0.0 DB.

LMS Case	Actual Location R_0 (m)	θ_0 (deg)	ψ_0 (deg)	Average Estimation Error $e_{R_{0x}}$ (m)	$e_{R_{0y}}$ (m)	e_{θ_0} (deg)	e_{ψ_0} (deg)	Range % Diff $e_{R_{0x}}$	$e_{R_{0y}}$
	$0.1*\rho$								
Flat	5.89	35.0	140.0	-0.192	-0.110	1.1	0.3	0.0	0.0
Curve	5.89	35.0	140.0	-0.009	-0.012	0.0	0.0	0.0	0.0
	$0.5*\rho$								
Flat	29.45	35.0	140.0	-0.356	0.078	0.0	0.0	-1.3	0.3
Curve	29.45	35.0	140.0	-0.926	-0.443	0.0	0.0	-3.1	-1.5
	$1.0*\rho$								
Flat	58.9	35.0	140.0	0.552	-0.856	0.0	0.0	0.9	-1.4
Curve	58.9	35.0	140.0	-3.47	0.230	0.0	0.0	-5.9	0.4
	$2.0*\rho$								
Flat	117.8	35.0	140.0	-3.23	-3.15	0.0	0.0	-2.7	-2.7
Curve	117.8	35.0	140.0	-75.9	-591	0.0	0.0	-64.4	-501
	$3.0*\rho$								
Flat	176.7	35.0	140.0	-23.6	-4.6	0.0	0.0	-13.3	-2.6
Curve	176.7	35.0	140.0	-63.7	-239	0.0	0.0	-36.1	-135
	$4.0*\rho$								
Flat	235.6	35.0	140.0	-25.2	-29.9	0.0	0.0	-25.0	-12.7
Curve	235.6	35.0	140.0	130.1	5273	0.0	0.0	55.2	2238

TABLE 6

CASE I.B.3- TARGET AT ARBITRARY POSITION, SINGLE HARMONIC, -3.0 DB.

	Actual Location			Average Estimation Error				Range % Diff	
LMS Case	R_0 (m)	θ_0 (deg)	ψ_0 (deg)	$e_{R_{0x}}$ (m)	$e_{R_{0y}}$ (m)	e_{θ_0} (deg)	e_{ψ_0} (deg)	$e_{R_{0x}}$	$e_{R_{0y}}$
	$\underline{0.1*\rho}$								
Flat	5.89	35.0	140.0	-0.190	-0.106	1.1	0.3	-3.2	-1.8
Curve	5.89	35.0	140.0	-0.019	-0.022	0.0	0.0	-0.3	-0.4
	$\underline{0.5*\rho}$								
Flat	29.45	35.0	140.0	-0.512	0.105	0.0	0.0	-1.7	0.4
Curve	29.45	35.0	140.0	-1.709	-0.782	0.0	0.0	-5.8	-2.7
	$\underline{1.0*\rho}$								
Flat	58.9	35.0	140.0	0.541	-1.379	0.0	0.0	0.9	-2.3
Curve	58.9	35.0	140.0	-8.69	-1.555	0.0	0.0	-14.8	-2.6
	$\underline{2.0*\rho}$								
Flat	117.8	35.0	140.0	-7.93	-7.07	0.0	0.0	-6.7	-6.0
Curve	117.8	35.0	140.0	128	16.6	0.0	0.0	109	14
	$\underline{3.0*\rho}$								
Flat	176.7	35.0	140.0	-50.4	-17.5	0.0	0.0	-28.5	-9.9
Curve	176.7	35.0	140.0	-174	-137	0.0	0.0	-98.7	-77.4
	$\underline{4.0*\rho}$								
Flat	235.6	35.0	140.0	-65.0	-413	0.0	0.0	-27.6	-175
Curve	235.6	35.0	140.0	474	359	0.0	0.0	161	122

the signal processing section of our analysis (in the absence of noise), the phase difference between two elements might deviate slightly above the maximum slope of the phase variation (π radians). The phase unwrapping algorithm classifies this phase difference as a wrap, even though one did not occur. The localization algorithm cannot properly process the phase data with this erroneous unwrapping. Conversely, the phase unwrapping algorithm might not detect an element where the phase had been wrapped. This unwrap anomaly only occurs at the highest harmonic when the target is located at endfire on an axis of the receive array.

The second limitation observed from this endfire case is more general in that it applies to all harmonics. Additionally, the discrepancy occurs when the target is located at a position endfire to the array, irrespective of the on-axis condition. Referring to Equation 2.77, which is one of the two equations essential for estimating the range, it can be seen that as the denominator approaches zero, the equation becomes invalid. Therefore, one limit of this equation is when twice the phase value at the center element, $\Theta_p(q,0,0)$, is equal to the sum of the phase values at the end elements, $\Theta_p(q,-m',0) + \Theta_p(q,m',0)$. This condition is approached when the target is located at a position endfire to the receive array.

Since the second limitation is more general than the unwrap anomaly, we chose to examine a target at an endfire

64

position off the array axis. Specifically, the bearing angle Ψ_0 chosen is equal to 237°. Additionally, we examined a target with three harmonics with a fundamental frequency of 1000 Hz. From Table 7, the no-noise case, we observe a discrepancy in the spherical coordinate estimates for LMS_{flat} in the extreme NF ($0.1*\rho_{min}$). Tables 8 and 9 document the performance of the algorithm in the presence of noise. Aside from the $0.1*\rho_{min}$ case for LMS_{flat}, both algorithms estimate the angular information satisfactorily. However, the range estimates of both algorithms using the phase values in the Y direction are erroneous. The phase variation curves shown in Figures 3.4 and 3.5 were generated for the highest frequency component (3000 Hz). By comparing the curvature in Figure 3.4 with that shown in Figure 3.5, we see that the phase variation along the Y axis is more linear. With near linear phase variation at endfire, the denominator of Equation 2.77 approaches zero.

In summary, this range estimation limitation only occurs at endfire geometries when a near-linear phase variation exists. The error introduced to the $\Theta_{q'}$ estimate (see Equation 2.75) is cancelled by the resulting error in range estimation (see Equation 2.76) such that the angular estimates are still valid (see Equations 2.79 and 2.80). This discrepancy combined with the unwrap deficiency outlined above are the only two limitations observed as we analyzed the full angular coverage capability of the algorithm.

TABLE 7

CASE I.C.1- TARGET AT ENDFIRE POSITION, THREE HARMONICS, NO NOISE.

q	Actual Location R_0 (m)	θ_0 (deg)	ψ_0 (deg)	Average Estimation Error $e_{R_{0x}}$ (m)	$e_{R_{0y}}$ (m)	e_{θ_0} (deg)	e_{ψ_0} (deg)	Range % Diff $e_{R_{0x}}$	$e_{R_{0y}}$
Flat	$0.1*\rho_{min}$								
1	0.654	90.0	237.0	-0.026	-0.163	33.5	3.66	-3.98	-24.9
2	0.654	90.0	237.0	-0.004	-0.151	31.9	4.34	-0.61	-23.1
3	0.654	90.0	237.0	-0.038	-0.567	45.4	16.7	-5.81	-86.7
Curve									
1	0.654	90.0	237.0	-0.008	0.019	0.0	-1.29	-1.22	2.91
2	0.654	90.0	237.0	0.000	0.027	0.0	-1.31	0.0	4.13
3	0.654	90.0	237.0	-0.001	0.026	0.0	-1.30	-0.15	3.98
Flat	$0.5*\rho_{min}$								
1	3.272	90.0	237.0	-0.206	-1.064	0.0	1.38	-6.30	-32.5
2	3.272	90.0	237.0	-0.448	-1.510	0.0	1.00	-13.7	-46.2
3	3.272	90.0	237.0	-4.159	9.435	0.0	-3.81	-127	288
Curve									
1	3.272	90.0	237.0	0.003	0.008	0.0	0.0	0.09	0.24
2	3.272	90.0	237.0	0.002	0.004	0.0	0.0	0.06	0.12
3	3.272	90.0	237.0	-0.001	-0.002	0.0	0.0	-0.03	-0.06
Flat	$1000*\rho_{max}$								
1	19635	90.0	237.0	48.7	-40.2	0.0	0.0	0.25	-0.20
2	19635	90.0	237.0	17.0	20.0	0.0	0.0	0.09	0.10
3	19635	90.0	237.0	-10.6	0.04	0.0	0.0	-0.05	0.00
Curve									
1	19635	90.0	237.0	-75.4	-53.9	0.0	0.0	-0.38	-0.27
2	19635	90.0	237.0	-10.3	45.0	0.0	0.0	-0.05	0.23
3	19635	90.0	237.0	-7.12	31.4	0.0	0.0	-0.04	0.16

TABLE 8

CASE I.C.2- TARGET AT ENDFIRE POSITION, THREE HARMONICS, 0.0 DB.

	Actual Location			Average Estimation Error				Range % Diff	
q	R_0 (m)	θ_0 (deg)	ψ_0 (deg)	$e_{R_{0x}}$ (m)	$e_{R_{0y}}$ (m)	e_{θ_0} (deg)	e_{ψ_0} (deg)	$e_{R_{0x}}$	$e_{R_{0y}}$
Flat	$0.1*\rho_{min}$								
1	0.654	90.0	237.0	-0.024	-0.170	33.6	3.82	-3.67	-26.0
2	0.654	90.0	237.0	-0.003	-0.149	30.5	4.38	-0.46	-22.8
3	0.654	90.0	237.0	-0.321	-0.006	42.0	11.4	-49.1	-0.92
Curve									
1	0.654	90.0	237.0	-0.002	-0.020	7.29	-1.53	-3.36	3.06
2	0.654	90.0	237.0	0.007	0.025	2.88	-0.98	1.07	3.82
3	0.654	90.0	237.0	-0.340	-0.922	35.2	16.3	-51.9	-140
Flat	$0.5*\rho_{min}$								
1	3.27	90.0	237.0	-0.209	-1.38	0.0	1.21	-6.39	-42.0
2	3.27	90.0	237.0	-0.401	-1.95	0.0	0.904	-12.3	-63.7
3	3.27	90.0	237.0	-3.14	-3.91	10.8	-0.866	-96.1	120
Curve									
1	3.27	90.0	237.0	-0.120	-1.88	3.34	-0.349	-3.67	-42.0
2	3.27	90.0	237.0	0.144	-1.95	2.67	-0.120	-4.40	-59.7
3	3.27	90.0	237.0	-0.027	-0.266	15.3	4.25	-0.83	-8.13
Flat	$1.0*\rho_{max}$								
1	19.6	90.0	237.0	-6.60	-5.91	1.24	-0.1	-33.6	-30.1
2	19.6	90.0	237.0	-1.33	-9.20	1.41	0.105	-6.77	-46.8
3	19.6	90.0	237.0	-0.22	-2.44	0.861	0.06	-1.12	-12.4
Curve									
1	19.6	90.0	237.0	23.8	16.9	5.27	-2.04	121	85.9
2	19.6	90.0	237.0	0.115	6.47	2.79	0.079	0.59	32.9
3	19.6	90.0	237.0	-1.85	14.6	12.0	2.32	-9.40	74.2
Flat	$3.0*\rho_{max}$								
1	58.9	90.0	237.0	-12.3	80.6	2.56	-0.14	-20.8	137
2	58.9	90.0	237.0	2.46	-140	1.62	-0.05	4.18	-238
3	58.9	90.0	237.0	-202	-157	1.72	-0.01	-343	-267
Curve									
1	58.9	90.0	237.0	49.4	56.5	3.69	-0.245	83.9	96.0
2	58.9	90.0	237.0	21.8	71.7	2.20	-0.180	37.0	122
3	58.9	90.0	237.0	-183	31.0	10.2	2.20	-310	52.7

TABLE 9

CASE I.C.3- TARGET AT ENDFIRE POSITION, THREE HARMONICS, -3.0 DB.

| q	Actual Location R_0 (m)	θ_0 (deg)	ψ_0 (deg)	Average Estimation Error $e_{R_{0x}}$ (m)	$e_{R_{0y}}$ (m)	e_{θ_0} (deg)	e_{ψ_0} (deg)	Range % Diff $e_{R_{0x}}$	$e_{R_{0y}}$
Flat	$0.1*\rho_{min}$								
1	0.654	90.0	237.0	-0.023	-0.173	33.5	3.90	-3.52	-26.0
2	0.654	90.0	237.0	-0.001	-0.144	28.6	4.30	-0.15	-22.8
3	0.654	90.0	237.0	-0.223	-0.076	42.5	4.97	-34.1	-0.92
Curve									
1	0.654	90.0	237.0	0.054	0.130	10.3	2.34	8.26	19.9
2	0.654	90.0	237.0	-0.041	-0.036	5.84	-0.65	-6.27	-5.50
3	0.654	90.0	237.0	-1.698	-1.613	44.2	16.5	-259	-246
Flat	$0.5*\rho_{min}$								
1	3.27	90.0	237.0	-0.230	-2.09	0.0	1.13	-7.03	-63.9
2	3.27	90.0	237.0	-0.988	-3.10	0.0	0.745	-30.2	-94.6
3	3.27	90.0	237.0	-3.11	3.93	17.4	0.912	-95.0	120
Curve									
1	3.27	90.0	237.0	-0.837	1.75	4.07	-0.483	-25.6	53.6
2	3.27	90.0	237.0	-0.275	-1.28	2.83	0.124	-8.40	-39.1
3	3.27	90.0	237.0	-8.51	0.843	24.5	7.59	-260	25.8
Flat	$1.0*\rho_{max}$								
1	19.6	90.0	237.0	-15.6	19.2	1.50	-0.107	-79.6	98.0
2	19.6	90.0	237.0	-2.88	38.9	1.74	0.133	-14.7	198
3	19.6	90.0	237.0	-0.569	36.4	1.13	0.068	-2.9	185
Curve									
1	19.6	90.0	237.0	20.6	11.7	8.38	-5.54	105	59.8
2	19.6	90.0	237.0	10.5	7.52	4.01	0.363	53.7	38.3
3	19.6	90.0	237.0	3.30	17.2	26.2	9.08	16.8	87.7
Flat	$3.0*\rho_{max}$								
1	58.9	90.0	237.0	-105	37.1	2.92	-0.209	-179	63.0
2	58.9	90.0	237.0	25.6	-31.6	1.88	-0.079	43.4	-53.6
3	58.9	90.0	237.0	-42.7	99.7	2.04	-0.012	-72.5	169
Curve									
1	58.9	90.0	237.0	77.5	133	4.38	-1.61	132	225
2	58.9	90.0	237.0	41.2	58.0	2.24	-0.087	70.0	98.5
3	58.9	90.0	237.0	67.1	-279	23.9	7.96	114	-472
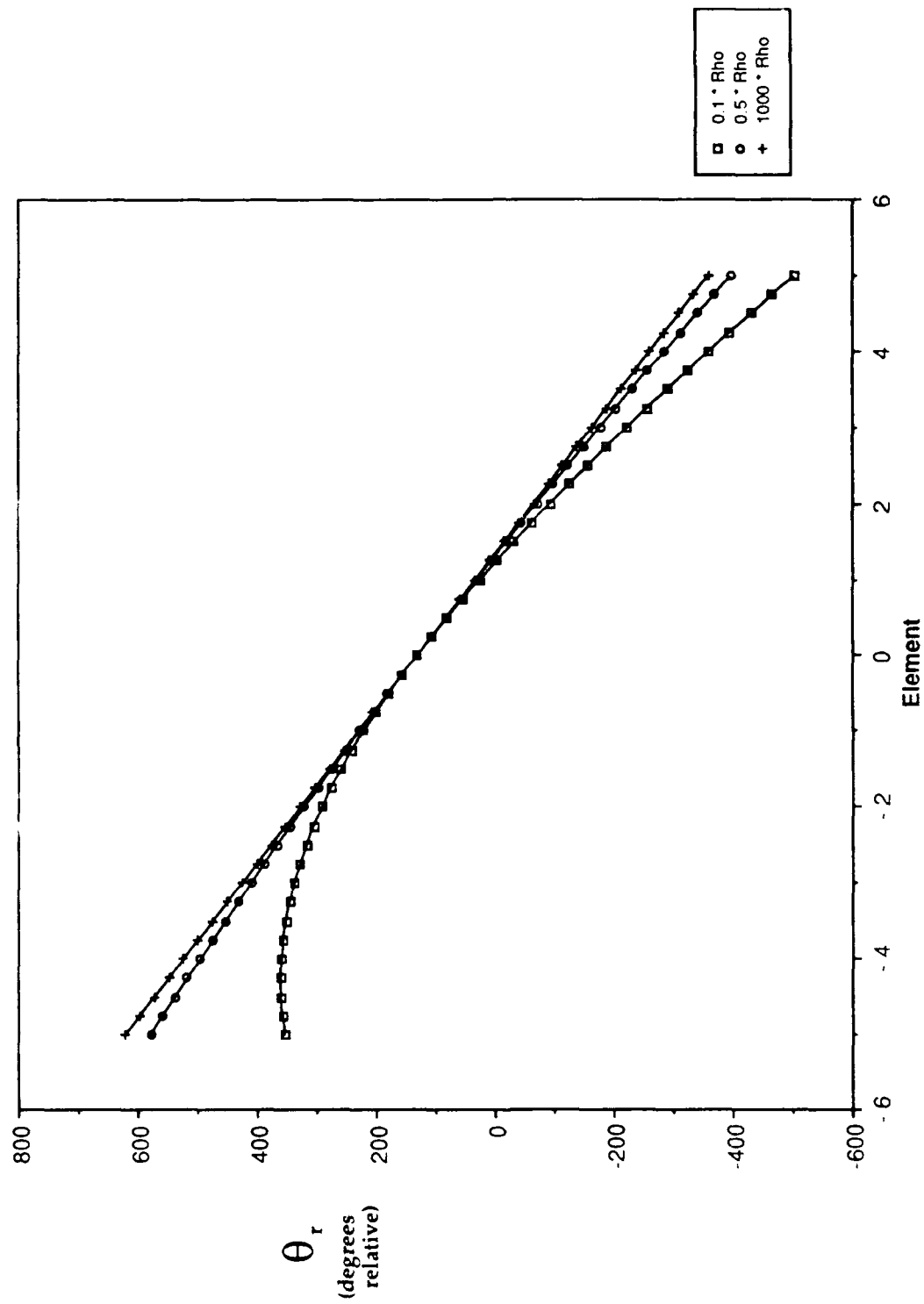
Figure 3.4 Phase Variation Across the X-axis as a Function of Range for Case IC.
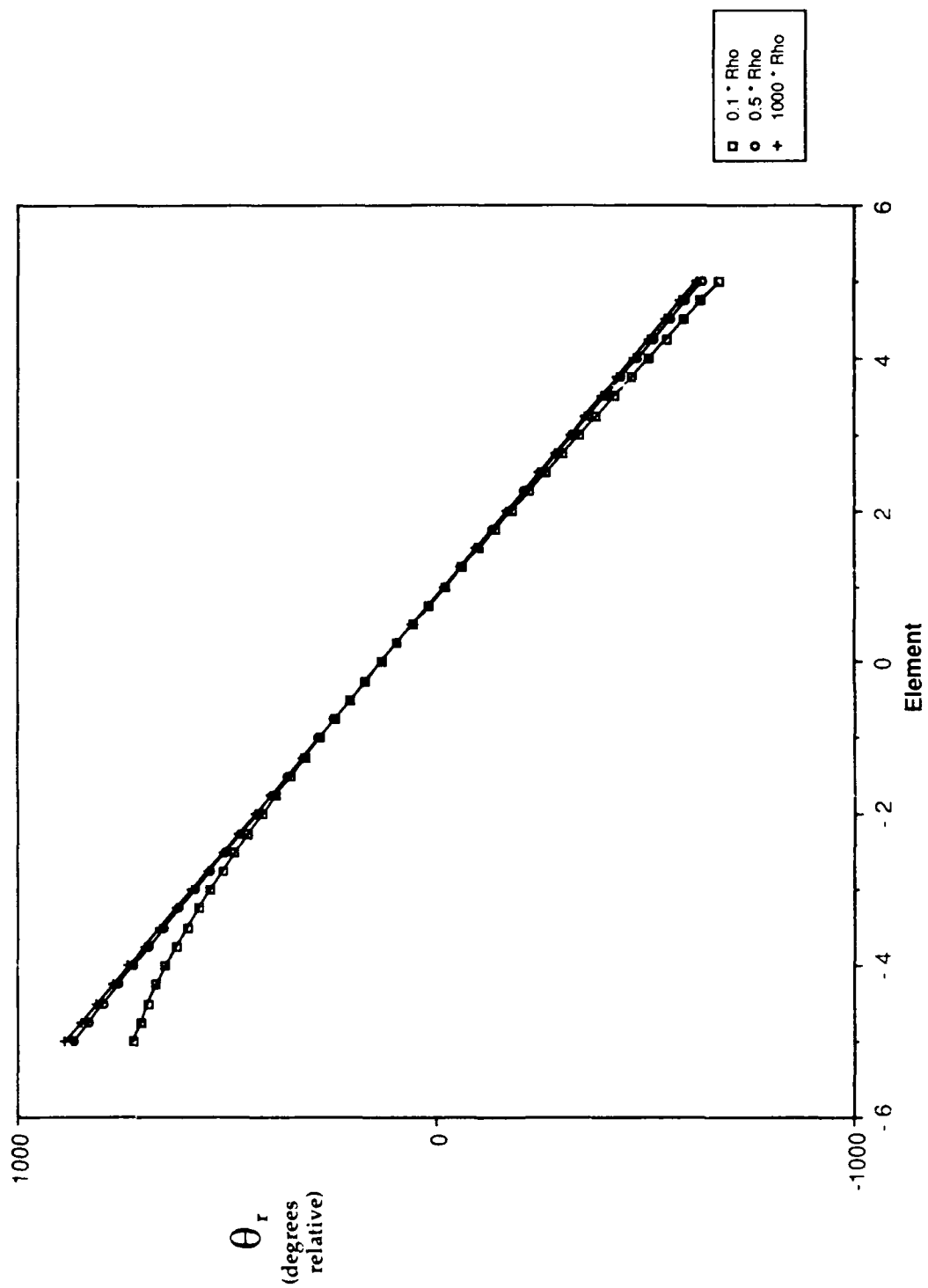
Figure 3.5   Phase Variation Across the Y-axis as a Function of Range for Case IC.

B. CATEGORY II: VALIDATION OF THE MULTI-HARMONIC CAPABILITY

The wavefront curvature, as measured at the surface of a receive array, is a function of a target's range (see Section II.B.2). In addition, the amount of wavefront curvature is also a function of the wavelength and thereby, frequency of the harmonic being processed. Given a target at a fixed position in space, for a given harmonic, the range value of the target can be represented by a constant times the range to the NF/FF boundary (const * ρ). As we analyze a target at a different harmonic, the value for the range to the NF/FF boundary (ρ) changes (see Equation 2.31). As we discuss the results of this section, we will occasionally refer to the range to the NF/FF boundary for a given harmonic as ρ_q, where q is the harmonic of interest. To describe this harmonic dependency of ρ, and the resultant relative position of the target to this ρ, consider the following example. Suppose a target has 10 harmonics to be analyzed in the frequency domain. Assume that at the highest harmonic, the range of the target can be specified as 0.1 * ρ_{10}. The range to the same target is equal to 1.0 * ρ_1 at the lowest harmonic. At the highest harmonic, the relative range to the target can be considered in the extreme near-field region. While, for the lowest harmonic, the relative range of the target is equal to ρ_1, the range to the NF/FF boundary. From this example, we see that a scenario could exist where a target may be considered as a NF target at one harmonic and a FF target at

another harmonic, even though the target remains at a fixed position in space.

In this case study, we analyze the performance of the two algorithms given a target that has many frequency components. In the first case, the target is located at a relative range of $0.56 * \rho_9$ (NF) at the highest harmonic. At the lowest harmonic, the relative position of the target is equal to 5 $* \rho_1$ (FF). The second example is chosen to represent a target with a relative range in the extreme NF at the highest component $(0.1 * \rho_7)$, to a relative range closer to the NF/FF boundary at the lowest component $(0.7 * \rho_1)$.

1.   Case II.A: Target With Nine Harmonics

In this test case, a fundamental frequency was chosen at 400 Hz. With nine harmonics, the band of the frequency spectrum varies from 400 to 3600 Hz. The results summarizing the performance of the two localization algorithms are presented in Tables 10 through 12. In the no-noise case (Table 10), the LMS_{curve} data reflects the dependence of the relative target position on frequency. At the lowest harmonic, where the target is at five times the relative NF/FF boundary $(5 * \rho_1)$, the range estimation error is largest. As harmonic number increases, the relative position of the target with respect to the ρ value at a given harmonic decreases. At the highest harmonic, the relative position of the target is in the NF and the range estimation error is the lowest. This effect is not evident in the LMS_{flat} results.

72

TABLE 10

CASE II.A.1- SINGLE TARGET, MULTI-HARMONIC (9), NO NOISE.

q	Actual Location			Average Estimation Error				Range % Diff	
	R_0 (m)	θ_0 (deg)	ψ_0 (deg)	$e_{R_{0x}}$ (m)	$e_{R_{0y}}$ (m)	e_{θ_0} (deg)	e_{ψ_0} (deg)	$e_{R_{0x}}$	$e_{R_{0y}}$
Flat	$5.0*\rho_{min}$								
1	9.09	5.0	310.0	-0.023	-0.023	0.013	-0.002	-0.25	-0.25
2	9.09	5.0	310.0	-0.023	-0.023	0.013	-0.001	-0.25	-0.25
3	9.09	5.0	310.0	-0.023	-0.023	0.013	-0.001	-0.25	-0.25
4	9.09	5.0	310.0	-0.023	-0.023	0.013	-0.001	-0.25	-0.25
5	9.09	5.0	310.0	-0.023	-0.023	0.013	-0.001	-0.25	-0.25
6	9.09	5.0	310.0	-0.023	-0.023	0.013	-0.001	-0.25	-0.25
7	9.09	5.0	310.0	-0.023	-0.023	0.013	-0.001	-0.25	-0.25
8	9.09	5.0	310.0	-0.023	-0.023	0.013	-0.001	-0.25	-0.25
9	9.09	5.0	310.0	-0.023	-0.023	0.013	-0.001	-0.25	-0.25
Curve	$5.0*\rho_{min}$								
1	9.09	5.0	310.0	0.004	0.004	-0.002	0.0	0.04	0.04
2	9.09	5.0	310.0	0.002	0.002	-0.001	0.0	0.02	0.02
3	9.09	5.0	310.0	0.001	0.001	-0.001	0.0	0.01	0.01
4	9.09	5.0	310.0	0.001	0.001	0.0	0.0	0.01	0.01
5	9.09	5.0	310.0	0.001	0.001	0.0	0.0	0.01	0.01
6	9.09	5.0	310.0	0.001	0.001	0.0	0.0	0.01	0.01
7	9.09	5.0	310.0	0.001	0.001	0.0	0.0	0.01	0.01
8	9.09	5.0	310.0	0.001	0.001	0.0	0.0	0.01	0.01
9	9.09	5.0	310.0	0.000	0.584	0.0	0.0	0.00	0.00

TABLE 11

CASE II.A.2- SINGLE TARGET, MULTI-HARMONIC (9), 0.0 DB.

q	Actual Location R_0 (m)	θ_0 (deg)	ψ_0 (deg)	Average Estimation Error $e_{R_{0x}}$ (m)	$e_{R_{0y}}$ (m)	e_{θ_0} (deg)	e_{ψ_0} (deg)	Range % Diff $e_{R_{0x}}$	$e_{R_{0y}}$
Flat	5.0*ρmin								
1	9.09	5.0	310.0	108	7.02	-0.559	3.00	1190	77.2
2	9.09	5.0	310.0	-11.0	-2.73	-0.311	2.48	-121	-30.1
3	9.09	5.0	310.0	-2.46	-1.28	0.010	-0.855	-27.1	-14.1
4	9.09	5.0	310.0	-1.18	-0.813	-0.096	-0.843	-13.0	-8.94
5	9.09	5.0	310.0	-0.350	-0.010	-0.017	0.524	-3.85	-0.11
6	9.09	5.0	310.0	-0.027	-0.094	0.032	0.268	-0.30	-1.03
7	9.09	5.0	310.0	-0.016	-0.225	0.007	-0.094	-0.18	-2.48
8	9.09	5.0	310.0	-0.143	-0.245	-0.003	0.829	-1.57	-2.70
9	9.09	5.0	310.0	-0.034	-0.289	0.017	-0.104	-0.37	-3.18
Curve	5.0*ρmin								
1	9.09	5.0	310.0	7.94	8.84	-4.72	93.5	87.3	97.2
2	9.09	5.0	310.0	8.91	9.91	-1.82	25.3	98.0	109
3	9.09	5.0	310.0	-7.64	1.60	-2.17	6.11	-84.1	17.6
4	9.09	5.0	310.0	1.60	-20.5	0.062	2.08	17.6	-226
5	9.09	5.0	310.0	-8.48	4.43	-0.164	2.10	-93.3	48.7
6	9.09	5.0	310.0	-2.05	-2.14	-0.093	-0.056	-22.6	-23.6
7	9.09	5.0	310.0	-5.19	-8.44	-0.079	-0.165	-57.1	-92.8
8	9.09	5.0	310.0	-8.85	0.207	-0.218	0.587	-97.4	2.28
9	9.09	5.0	310.0	-1.77	0.584	-0.364	0.605	-19.4	6.42

TABLE 12

CASE II.A.3- SINGLE TARGET, MULTI-HARMONIC (9), -3.0 DB.

q	Actual Location R_0 (m)	θ_0 (deg)	ψ_0 (deg)	Average Estimation Error $e_{R_{0x}}$ (m)	$e_{R_{0y}}$ (m)	e_{θ_0} (deg)	e_{ψ_0} (deg)	Range % Diff $e_{R_{0x}}$	$e_{R_{0y}}$
Flat	$5.0*\rho_{min}$								
1	9.09	5.0	310.0	7.97	-16.3	-1.05	25.5	87.7	-179
2	9.09	5.0	310.0	-10.6	16.0	-0.526	3.55	-116	176
3	9.09	5.0	310.0	-4.14	-5.91	-0.010	-1.35	-45.6	-65.0
4	9.09	5.0	310.0	-3.29	-2.70	-0.155	-1.19	-36.2	-29.7
5	9.09	5.0	310.0	1.41	-0.218	-0.039	0.682	-15.6	-2.40
6	9.09	5.0	310.0	-0.114	-0.336	0.033	0.319	-1.25	-3.70
7	9.09	5.0	310.0	-0.110	-0.427	0.002	-0.051	-1.21	-4.70
8	9.09	5.0	310.0	-0.279	-0.550	-0.013	1.21	-3.07	-6.05
9	9.09	5.0	310.0	-0.149	-0.511	0.018	-0.154	-1.64	-5.62
Curve	$5.0*\rho_{min}$								
1	9.09	5.0	310.0	11.5	8.88	-17.4	102	127	97.7
2	9.09	5.0	310.0	0.088	10.0	-8.21	53.3	0.97	110
3	9.09	5.0	310.0	2.38	106	-8.00	39.4	26.2	1171
4	9.09	5.0	310.0	-89.8	18.8	-2.17	26.4	-988	207
5	9.09	5.0	310.0	-2.24	-1.62	-1.31	12.5	-24.6	-17.8
6	9.09	5.0	310.0	5.30	-4.04	-2.99	21.5	58.3	-44.4
7	9.09	5.0	310.0	-1.40	1.93	-2.83	13.5	-15.4	21.2
8	9.09	5.0	310.0	15.4	-3.40	-0.526	2.11	170	-37.4
9	9.09	5.0	310.0	-1.75	-4.53	-1.07	16.7	-19.2	-49.9

Figure 3.6 describes the phase variation across the X axis for three harmonics. At the highest harmonic, the wavefront curvature is most significant; whereas, for the lowest component, the curvature is minimal. The test case results for the scenarios with noise corruption are presented in Tables 11 and 12. In general, LMS_{flat} performs the best over the wide range of frequencies. For the lowest three harmonics, neither algorithm provides an adequate range estimate.

2. Case II.B: Target With Seven Harmonics

In this case, we examine a target with a range value equal to $0.7 * \rho_1$. The fundamental frequency is 400 Hz and the band of the frequency spectrum covers 400 to 2800 Hz. Since the lowest harmonic describes the maximum relative range of the target to the NF/FF boundary, the relative ranges at every harmonic will be within the NF. This case was chosen to demonstrate the performance of both LMS algorithms at each harmonic. As was previously discussed, LMS_{flat} should perform best in cases with minimal wavefront curvature. The converse is true for LMS_{curve}. A different bearing and depression angle were chosen for this case.

The trends discussed in the last section are evident in the results presented in Tables 13 through 15 for this case. In the noise cases (Tables 14 and 15), LMS_{flat} gives a better range estimate for the first two harmonics than the LMS_{curve} estimates. LMS_{curve} performs best for the higher
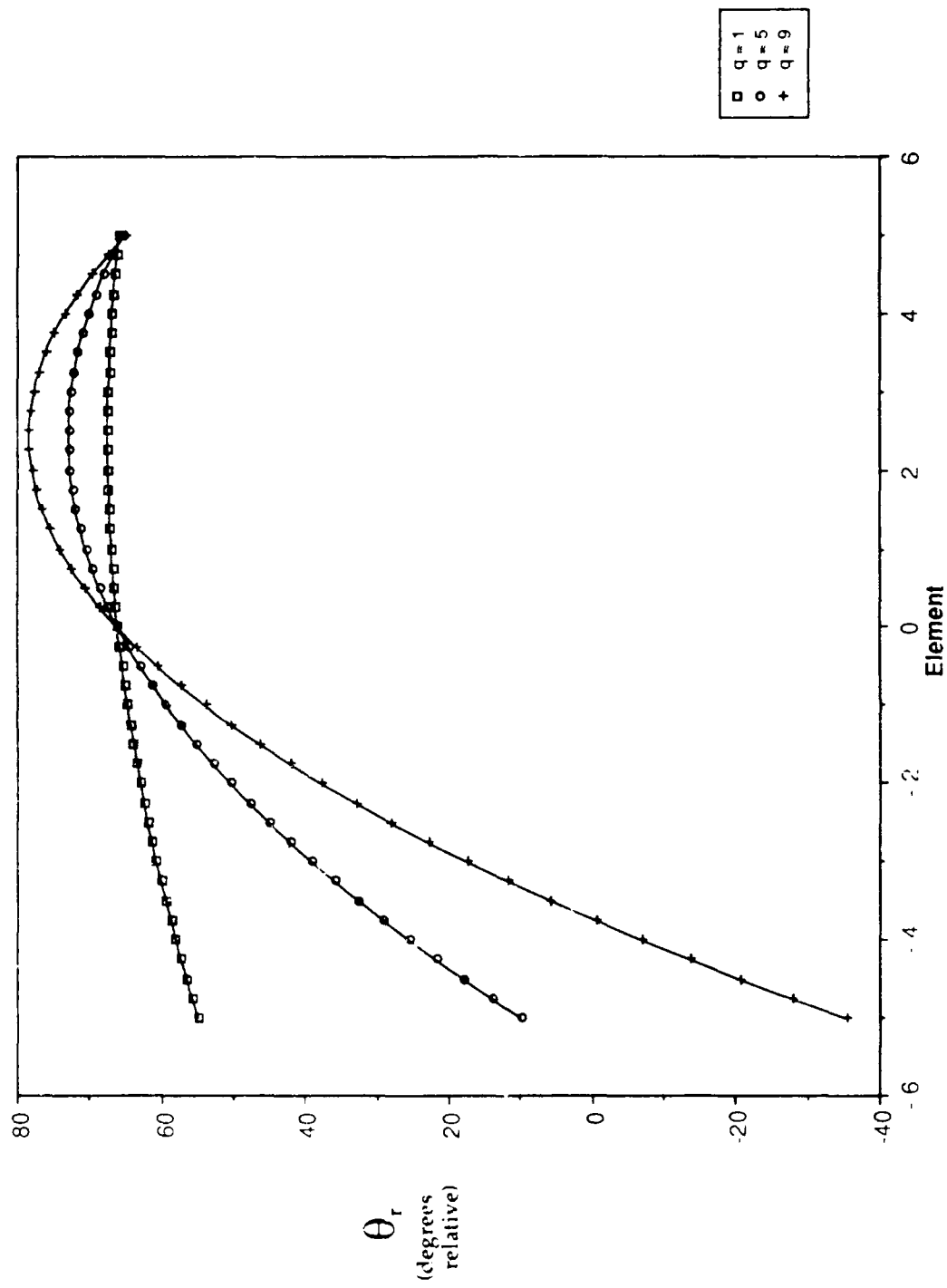
76

Figure 3.6 Phase Variation Across the X-axis as a Function of Harmonic q for Case IIA.

TABLE 13

CASE II.B.1- SINGLE TARGET, MULTI-HARMONIC (7), NO NOISE.

q	Actual Location			Average Estimation Error				Range % Diff	
	R_0 (m)	θ_0 (deg)	ψ_0 (deg)	$e_{R_{0x}}$ (m)	$e_{R_{0y}}$ (m)	$\bar{e}_{\theta_0}$ (deg)	e_{ψ_0} (deg)	$e_{R_{0x}}$	$e_{R_{0y}}$
Flat	$0.7*\rho_{min}$								
1	2.104	23.0	129.0	-0.109	-0.125	1.285	-0.177	-5.18	-5.94
2	2.104	23.0	129.0	-0.109	-0.124	1.283	-0.175	-5.18	-5.89
3	2.104	23.0	129.0	-0.108	-0.124	1.279	-0.174	-5.13	-5.89
4	2.104	23.0	129.0	-0.107	-0.123	1.274	-0.171	-5.09	-5.85
5	2.104	23.0	129.0	-0.106	-0.122	1.265	-0.173	-5.04	-5.80
6	2.104	23.0	129.0	-0.105	-0.120	1.254	-0.175	-4.99	-5.70
7	2.104	23.0	129.0	-0.103	-0.118	1.241	-0.178	-4.90	-5.61
Curve	$0.7*\rho_{min}$								
1	2.104	23.0	129.0	0.005	0.005	-0.037	0.1	0.24	0.24
2	2.104	23.0	129.0	0.002	0.002	-0.004	0.1	0.10	0.10
3	2.104	23.0	129.0	0.001	0.001	0.007	0.1	0.05	0.05
4	2.104	23.0	129.0	-0.002	-0.002	0.045	0.1	-0.10	-0.10
5	2.104	23.0	129.0	-0.002	-0.002	0.042	0.1	-0.10	-0.10
6	2.104	23.0	129.0	-0.002	-0.002	0.040	0.1	-0.10	-0.10
7	2.104	23.0	129.0	-0.002	-0.002	0.038	0.1	-0.10	-0.10

TABLE 14

CASE II.B.2- SINGLE TARGET, MULTI-HARMONIC (7), 0.0 DB.

	Actual Location			Average Estimation Error				Range % Diff	
q	R_0 (m)	θ_0 (deg)	ψ_0 (deg)	$e_{R_{0x}}$ (m)	$e_{R_{0y}}$ (m)	e_{θ_0} (deg)	e_{ψ_0} (deg)	$e_{R_{0x}}$	$e_{R_{0y}}$
Flat	$0.7*\rho_{min}$								
1	2.104	23.0	129.0	-0.171	-0.220	1.395	-0.130	-8.13	-10.5
2	2.104	23.0	129.0	-0.171	-0.130	1.367	0.214	-8.13	-6.18
3	2.104	23.0	129.0	-0.116	-0.131	1.279	0.161	-5.51	-6.23
4	2.104	23.0	129.0	-0.104	-0.119	1.163	-0.169	-4.94	-5.66
5	2.104	23.0	129.0	-0.106	-0.135	1.231	-0.286	-5.04	-6.42
6	2.104	23.0	129.0	-0.115	-0.121	1.280	-0.088	-5.47	-5.75
7	2.104	23.0	129.0	-0.102	-0.125	1.240	-0.229	-4.85	-5.94
Curve	$0.7*\rho_{min}$								
1	2.104	23.0	129.0	-0.988	0.338	-1.78	2.31	-47.0	16.1
2	2.104	23.0	129.0	-0.356	-0.323	-0.506	2.35	-16.9	-15.4
3	2.104	23.0	129.0	-0.016	-0.076	-0.022	-1.36	-0.76	-3.61
4	2.104	23.0	129.0	0.058	0.153	-4.29	-3.11	2.76	7.27
5	2.104	23.0	129.0	-0.028	-0.002	-1.40	1.09	-1.33	2.99
6	2.104	23.0	129.0	-0.063	-0.063	-0.006	-0.008	-2.99	-1.57
7	2.104	23.0	129.0	-0.020	-0.214	0.29	-0.447	-0.95	-10.2

TABLE 15

CASE II.B.3- SINGLE TARGET, MULTI-HARMONIC (7), -3.0 DB.

q	Actual Location			Average Estimation Error				Range % Diff	
	R_0 (m)	θ_0 (deg)	ψ_0 (deg)	$e_{R_{0x}}$ (m)	$e_{R_{0y}}$ (m)	e_{θ_0} (deg)	e_{ψ_0} (deg)	$e_{R_{0x}}$	$e_{R_{0y}}$
Flat	$0.7*\rho_{min}$								
1	2.104	23.0	129.0	-0.238	-0.292	1.385	-0.095	-11.3	-17.9
2	2.104	23.0	129.0	-0.204	-0.139	1.380	0.387	-9.70	-6.61
3	2.104	23.0	129.0	-0.122	-0.135	1.264	0.298	-5.80	-6.42
4	2.104	23.0	129.0	-0.105	-0.119	1.113	-0.159	-4.99	-5.66
5	2.104	23.0	129.0	-0.108	-0.142	1.211	-0.328	-5.13	-6.75
6	2.104	23.0	129.0	-0.120	-0.123	1.289	-0.056	-5.70	-5.85
7	2.104	23.0	129.0	-0.103	-0.128	1.240	-0.250	-4.90	-6.08
Curve	$0.7*\rho_{min}$								
1	2.104	23.0	129.0	-6.38	-0.471	-6.13	4.58	-303	-22.4
2	2.104	23.0	129.0	2.35	-0.174	-5.37	6.89	112	-8.27
3	2.104	23.0	129.0	-0.050	0.093	-3.22	-7.16	-2.38	4.42
4	2.104	23.0	129.0	0.373	3.67	-7.79	-3.96	17.7	17.4
5	2.104	23.0	129.0	-0.088	-0.074	-4.26	-2.52	-4.18	-3.52
6	2.104	23.0	129.0	-0.268	-0.578	-2.36	1.95	-12.7	-27.5
7	2.104	23.0	129.0	-1.94	-0.590	-0.792	1.09	-92.2	-28.0

harmonics. The phase variation for harmonics three through seven contain significant wavefront curvature as seen in Figure 3.7. Harmonics one and two have minimal wavefront curvature. This case demonstrates the regions where one LMS algorithm is superior to the other.

C. CATEGORY III: VALIDATION OF THE MULTIPLE TARGET CAPABILITY

In this final section, the performance of the two algorithms is evaluated in a multiple target, multiple harmonic case. Three targets are oriented at random geometries in both the NF and FF regions. Each target radiates two unique spectral lines resulting in six total harmonics. A fundamental frequency of 100 Hz was chosen. Therefore, the band of the frequency spectrum is 100 to 700 Hz. Many factors affect the amount of wavefront curvature for a given harmonic. This test case shows the complexities involved in analyzing a target when several of the wavefront curvature limiting effects are combined. Two major factors are evident as we analyze the multiple targets in this scenario. First, as a target's depression angle increases from the broadside position, the amount of wavefront curvature becomes less significant. Secondly, as we analyze data at lower harmonics, the wavefront curvature is also less. These two factors were examined individually in Sections III.A.3 and Section III.B.
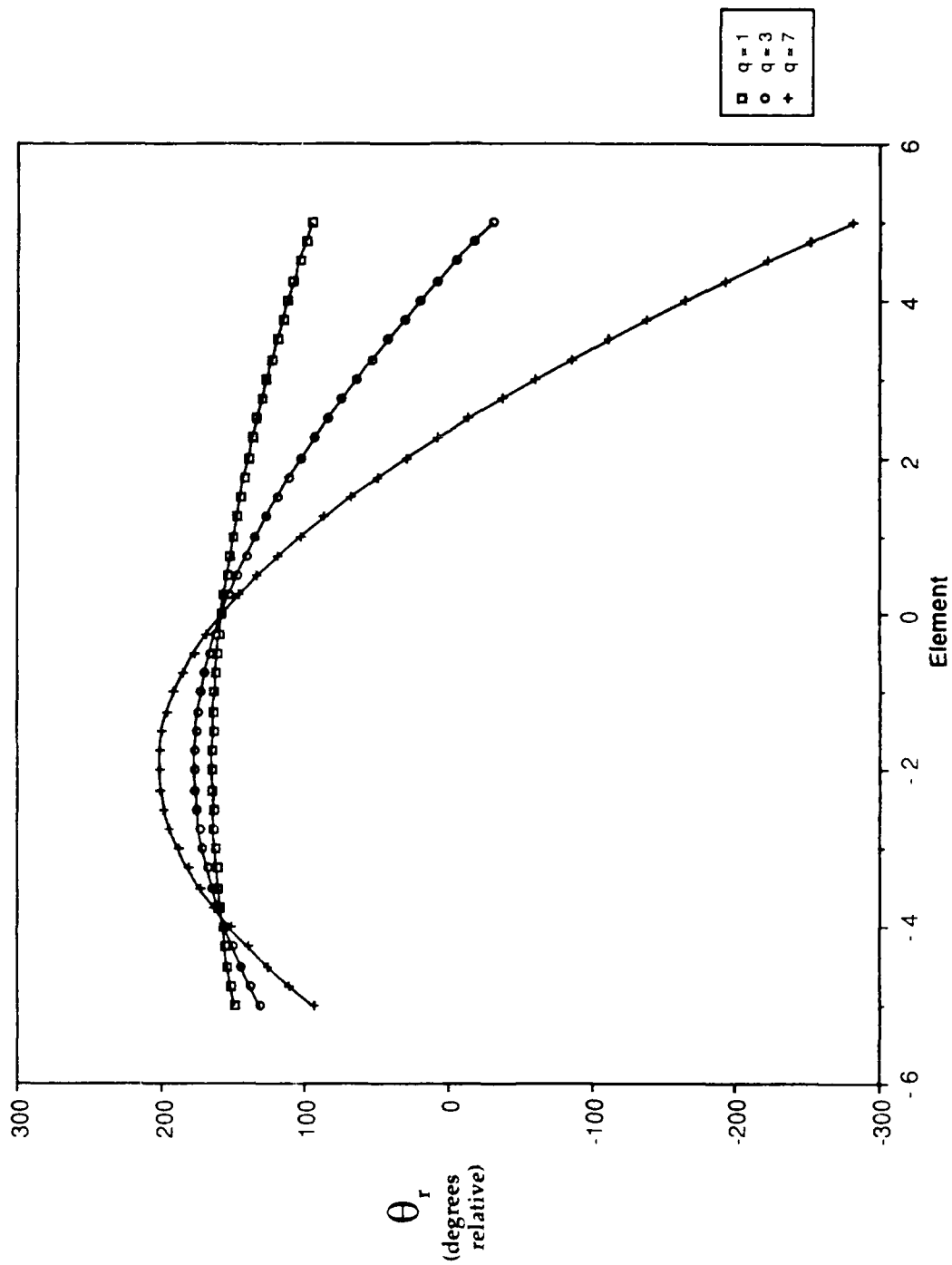
Figure 3.7 Phase Variation Across the X-axis as a Function of Harmonic q for Case IIB.

Target 1 is located in the near field ($0.3 * \rho_{min}$) at $\Theta_o = 42°$ and $\Psi = 153°$ and radiates harmonics 1 and 3. Target 2 is closer to the NF/FF boundary ($1.8 * \rho_{min}$) at $\Theta_o = 71'$ and $\Psi = 218°$ (harmonics 2 and 5). The final target is in the FF ($3.0 * \rho_{max}$) at $\Theta_o = 2°$ and $\Psi = 47°$ (harmonics 4 and 6). In order to prevent the FF target from being masked by the noise levels of the other targets, the initial magnitude of the Fourier series coefficients were weighted so that the signal strength of each target at the receive array would be equal. We will summarize the results in Tables 16 through 18 by considering the targets one at a time.

From Table 16, in the absence of noise, the LMS_{curve} routine localizes Target 1 with minimal estimation errors. However, in a noise environment (see Tables 17 and 18), LMS_{flat} yields a more accurate estimate of the spherical coordinates at both harmonics. Given the phase variation shown in Figure 3.8, it is clear that at both harmonics, significant wavefront curvature is present. Under these conditions, LMS_{curve} should perform better than LMS_{flat}, but it does not.

This performance discrepancy can be attributed in part to the design of the array. Since the interelement spacing is optimally designed for the highest frequency of interest, the performance of the localization algorithm at lower frequencies is degraded. The results recorded in Table 16 bear witness to this fact. The range estimation error is maximum at the lowest harmonic. A similar trend was also observed in the

83

TABLE 16

CASE III- MULTI-TARGET (3), MULTI-HARMONIC (6), NO NOISE.

q	Actual Location			Average Estimation Error				Range % Diff	
	R_0 (m)	θ_0 (deg)	ψ_0 (deg)	$e_{R_{0x}}$ (m)	$e_{R_{0y}}$ (m)	e_{θ_0} (deg)	e_{ψ_0} (deg)	$e_{R_{0x}}$	$e_{R_{0y}}$
Flat									
1	9.817	42.0	153.0	-0.659	0.039	1.81	1.35	-6.71	0.40
2	58.90	71.0	218.0	-0.685	-0.294	-0.411	-0.067	-1.16	-0.50
3	9.817	42.0	153.0	-0.619	0.066	1.72	1.36	-6.31	0.67
4	294.5	2.0	47.0	-0.026	-0.026	0.00	0.00	-0.01	-0.01
5	58.90	71.0	218.0	-0.707	-0.302	-0.411	-0.066	-1.20	-0.51
6	294.5	2.0	47.0	-0.026	-0.026	0.00	0.00	-0.01	-0.01
Curve									
1	9.817	42.0	153.0	0.040	0.020	-0.132	-0.042	0.41	0.20
2	58.90	71.0	218.0	0.028	0.016	-0.023	0.00	0.05	0.03
3	9.817	42.0	153.0	-0.005	-0.011	0.021	-0.041	-0.05	-0.11
4	294.5	2.0	47.0	0.004	0.004	0.00	0.00	0.00	0.00
5	58.90	71.0	218.0	-0.011	-0.006	0.009	0.00	-0.02	-0.01
6	294.5	2.0	47.0	0.002	0.002	0.00	0.00	0.00	0.00

TABLE 17

CASE III- MULTI-TARGET (3), MULTI-HARMONIC (6), 0.0 DB.

q	Actual Location R_0 (m)	θ_0 (deg)	ψ_0 (deg)	Average Estimation Error $e_{R_{0x}}$ (m)	$e_{R_{0y}}$ (m)	e_{θ_0} (deg)	e_{ψ_0} (deg)	Range % Diff $e_{R_{0x}}$	$e_{R_{0y}}$
Flat									
1	9.817	42.0	153.0	-1.19	-0.275	1.99	1.29	-12.1	-2.8
2	58.90	71.0	218.0	-72.5	-18.8	-0.596	-0.10	-123	-32.1
3	9.817	42.0	153.0	-0.542	0.051	1.58	1.46	-5.52	0.52
4	294.5	2.0	47.0	626	-53.1	-0.044	-0.270	213	-18.0
5	58.90	71.0	218.0	-2.96	-2.52	-0.301	-0.047	-5.02	-4.27
6	294.5	2.0	47.0	-11.2	-26.3	0.037	0.107	-3.80	-8.94
Curve									
1	9.817	42.0	153.0	-3.47	9.84	-3.57	-0.453	-35.3	100
2	58.90	71.0	218.0	31.8	165	-1.18	0.168	54.1	280
3	9.817	42.0	153.0	1.83	0.918	-3.85	4.09	18.7	9.35
4	294.5	2.0	47.0	276	301	-0.255	-32.2	93.8	102
5	58.90	71.0	218.0	146	-34.0	0.723	-0.214	248	-57.7
6	294.5	2.0	47.0	-8.03	-10.4	-0.145	-2.52	-2.3	-3.54

TABLE 18

CASE III- MULTI-TARGET (3), MULTI-HARMONIC (6), -3.0 DB.

| q	Actual Location R_0 (m)	θ_0 (deg)	ψ_0 (deg)	Average Estimation Error $e_{R_{0x}}$ (m)	$e_{R_{0y}}$ (m)	e_{θ_0} (deg)	e_{ψ_0} (deg)	Range % Diff $e_{R_{0x}}$	$e_{R_{0y}}$
Flat									
1	9.817	42.0	153.0	-1.74	-0.488	1.85	1.32	-17.7	-4.97
2	58.90	71.0	218.0	160	21.5	-0.794	-0.112	271	36.5
3	9.817	42.0	153.0	-0.549	0.023	1.52	1.49	-5.59	0.23
4	294.5	2.0	47.0	497	145.7	-0.070	-0.241	168	49.5
5	58.90	71.0	218.0	-7.30	-4.91	-0.280	-0.038	-12.4	-8.34
6	294.5	2.0	47.0	-242	12700	0.050	0.055	-82.2	4303
Curve									
1	9.817	42.0	153.0	-1.52	6.65	-9.80	2.32	-15.5	67.8
2	58.90	71.0	218.0	41.3	50.9	1.33	-0.747	70.1	86.4
3	9.817	42.0	153.0	5.28	1.04	-6.65	16.5	53.8	10.6
4	294.5	2.0	47.0	-29.1	228	-1.30	-53.1	-9.88	77.6
5	58.90	71.0	218.0	22.1	5.59	9.48	-2.84	37.5	9.49
6	294.5	2.0	47.0	53.6	419	-0.256	-15.6	18.2	142
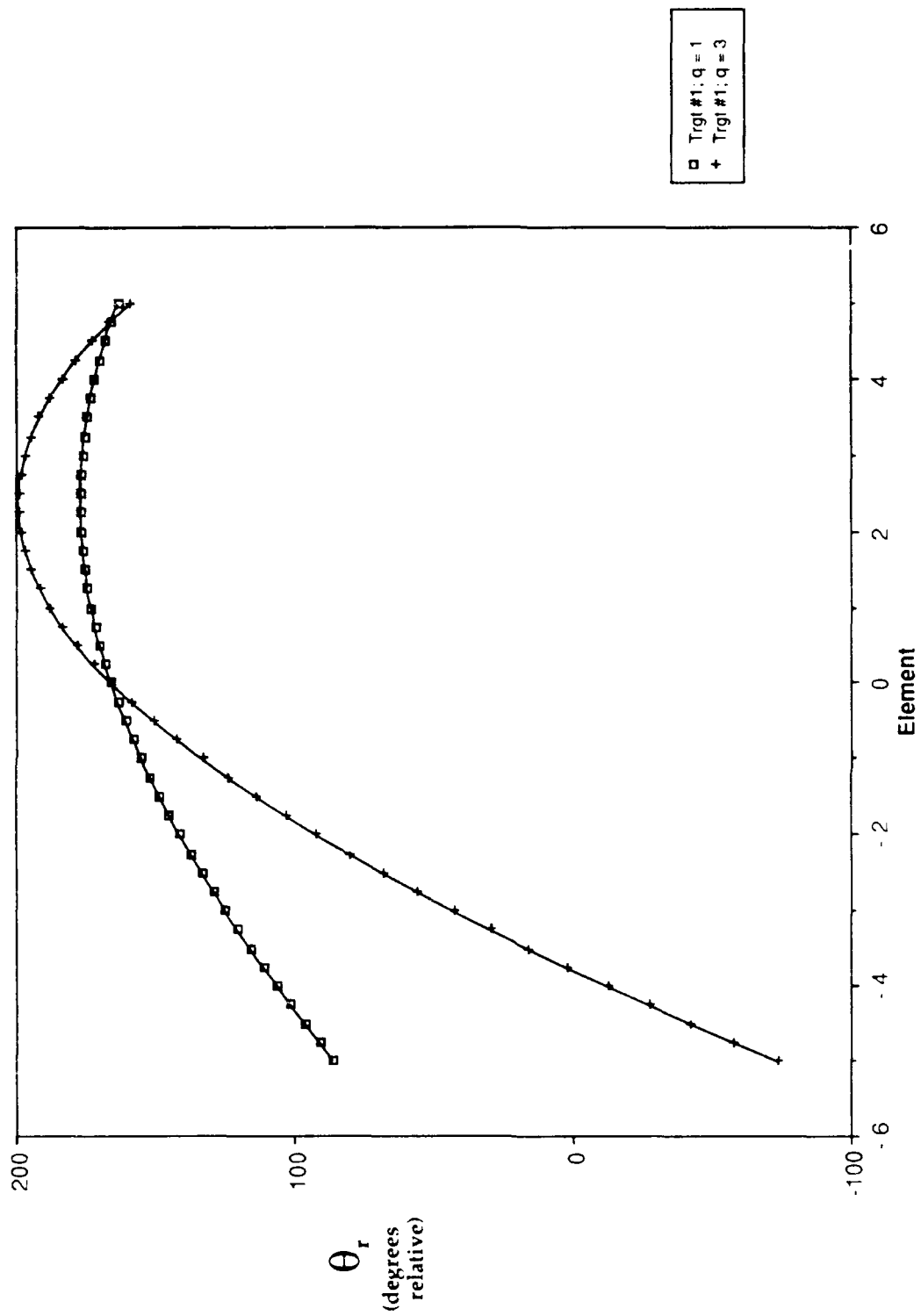
Figure 3.8 Phase Variation Across the Y-axis as a Function of Harmonic q for Case III: Target #1.

single target, multiple harmonic cases in Section III.B (see Tables 10 and 13). Although the wavefront curvature is minimal at the lowest harmonic, another contribution to the increase in range estimation error at the lower harmonics is the inefficiency introduced from the array design.

From Tables 17 and 18, it appears that the LMS_{curve} algorithm is more sensitive to the inefficient array design at the lower harmonics. In the single harmonic test cases previously discussed (Section III.A), the maximum reliable range estimate determined by the LMS_{curve} algorithm for the 0.0 dB noise case was approximately $1.0 * \rho$. Whereas, for the same conditions, the LMS_{flat} algorithm could adequately determine a range estimate out to a range value of $3.0 * \rho$. Given a scenario with an increased number of harmonics, this disparity in the maximum range estimate performance of the two algorithms is amplified at lower harmonics. As a result, even through Target 1 exhibits significant wavefront curvature, the LMS_{curve} algorithm does not efficiently analyze the target at the low harmonics (q = 1,3).

The wavefront curvature of Target 2 is negligible at both of its harmonics, q = 2,5. The major cause for this is the depression angle Θ_o. Target 2 is located at a depression angle $\Theta_o = 71°$. This target, although positioned at the NF/FF interface region, is located close to endfire. As a result, the phase variation across the Y axis is negligible (see Figure 3.9). The LMS_{curve} algorithm cannot correctly estimate
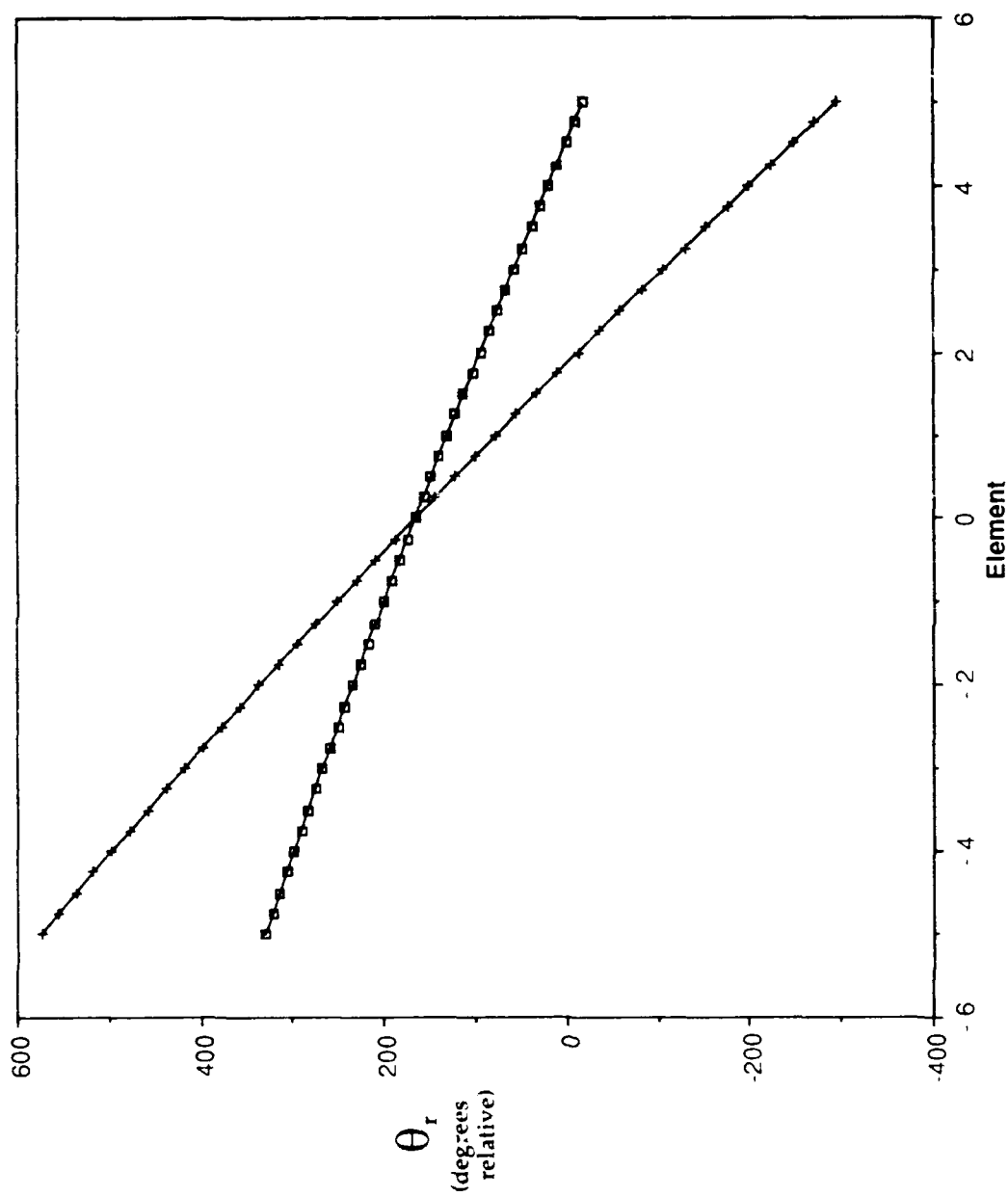
Figure 3.9 Phase Variation Across the Y-axis as a Function of Harmonic q for Case III: Target #2.

the range of a target given this minimal wavefront curvature. At the higher harmonic (q=5), the LMS_{flat} algorithm gives a good range estimate for this target.

Target 3, the target located in the FF region, radiates harmonics q = 4,6. For the 0.0 dB case (refer to Table 17), LMS_{curve} produces a good estimate at the highest harmonic q = 6. Both algorithms perform poorly for this target at q = 4. From Figure 3.10 it can be seen that significant wavefront curvature is evident at these harmonics even with the target positioned in the far-field. As seen in our earlier results, this can be attributed to the near broadside orientation of the target relative to the array (Θ_o = 2°). The superior performance of LMS_{curve} at this harmonic, can be attributed to significant wavefront curvature coupled with the fact that the array design is optimized at this highest harmonic. The LMS_{flat} algorithm adequately estimates the target range at harmonic 6. In summary, this case is the most complex to analyze in that several factors must be considered simultaneously at each harmonic to evaluate algorithm performance. At low harmonics, the performance of the LMS_{flat} algorithm is slightly superior to that of LMS_{curve} for the given targets. The LMS_{curve} algorithm performed better than LMS_{flat} at the highest harmonic for the target near broadside. Target 2 generates minimal wavefront curvature and was most difficult to localize in range. All angular estimates were within five degrees for the 0.0 dB noise case and 10 degrees for -3.0 dB.
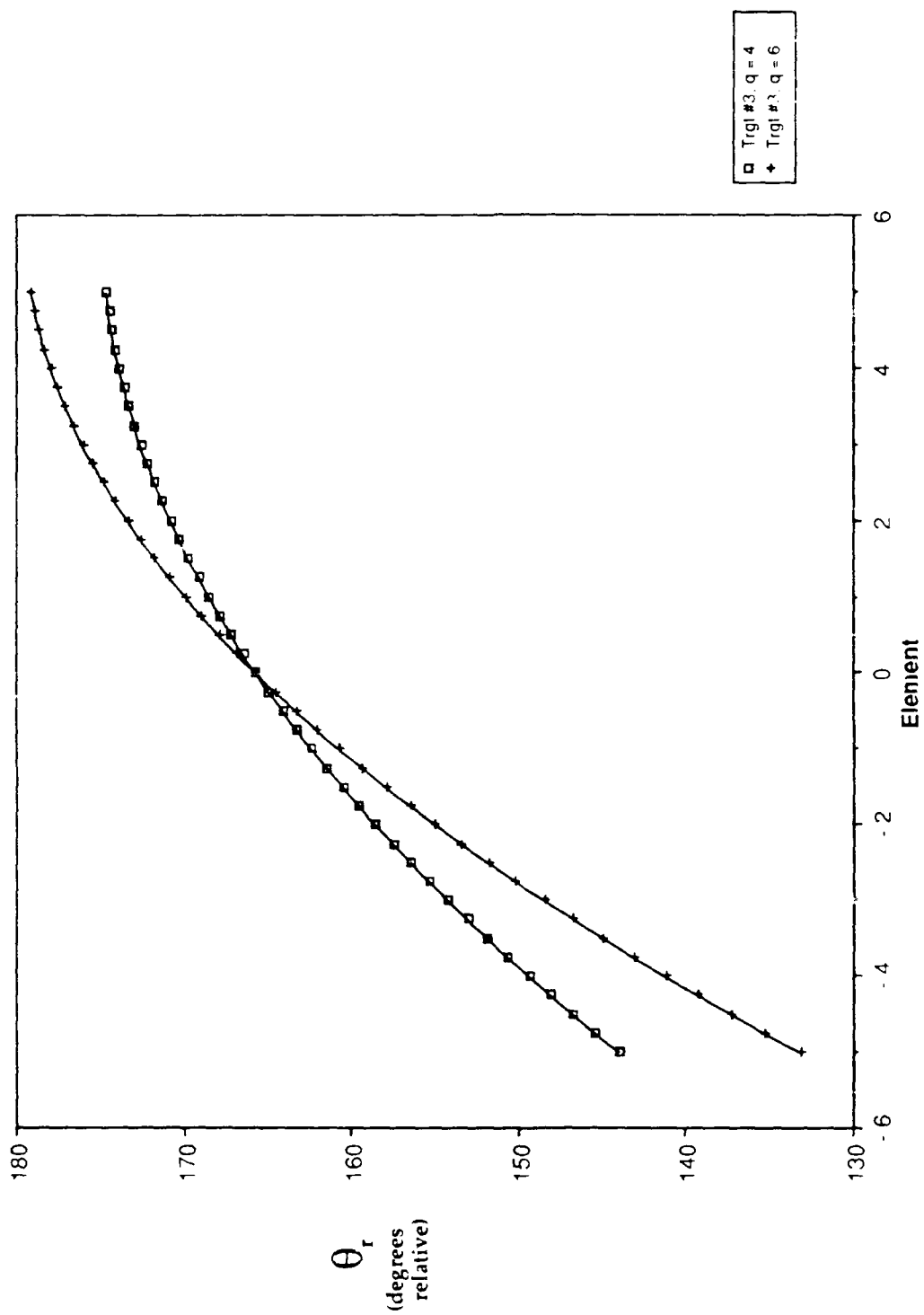
Figure 3.10   Phase Variation Across the Y-axis as a Function of Harmonic q for Case III: Target #3.

IV. CONCLUSIONS AND RECOMMENDATIONS

The purpose of this thesis was to develop a localization algorithm that could process spherical wave information incident upon a planar array and estimate the three spherical coordinates range r_o, depression angle θ_o, and bearing angle Ψ_o. This goal has been achieved by the signal processing model described in Section II.B and the localization algorithm outlined in Section II.C. Two different modified frequency-domain LMS adaptive algorithms were used to cancel the noise corruption of the output electrical signals. A comparison of the performance of each of these adaptive algorithms was detailed in the results section (Section III). The following comments highlight the significant findings from our results:

- The spherical wave propagation model used in generating the ouput electrical signals at each element in a planar array has been validated.

- The adaptive beamforming and non-linear least-squares estimation routines used in the signal processing section have been tested satisfactorily in a no-noise and noise environment.

- In the absence of noise, or in high SNR cases, the localization models using both modified LMS adaptive algorithms accurately estimate range well into the far-field region.

- Regardless of range estimation performance, both algorithms accurately estimated the bearing and depression angles in all cases tested.

- In a noisy environment, for a signal target, the routine that assumed non-separable phase weights in the LMS algorithm performed best given a wavefront with significant wavefront curvature.

92

- In a noisy environment, for a single target, the routine that assumed separable phase weights in the LMS algorithm performed best given minimal wavefront curvature. As a result, this routine could estimate the range to targets positioned at further distances from the receive array. Also, this routine was superior in estimating the range value at lower harmonics. Range estimates into the far-field were accurately determined by this algorithm in a noise environment.

- Aside from the case where the target is located at an endfire position relative to the receive array, the full angular coverage capability of the algorithm was tested satisfactorily.

- The ability to process several harmonics over the frequency spectrum of a single, broadband target was tested satisfactorily.

- Given multiple targets positioned in both the near-field and far-field with unique spectral lines, both algorithms determined adequate estimates of the spherical coordinates for these targets in a noise environment.

Given the design limitations presented in the introduction to Section III, the following trend was observed in the maximum range estimate capability of the separable weight routine LMS_{flat}: In a noise environment characterized by a SNR value of 0.0 dB, the range estimate is valid to a distance of three times the range to the near-field/far-field boundary. For an 11 × 11 element array designed to process a maximum frequency of 1000 Hz, the planar array dimensions would be 7 meters × 7 meters. The maximum range estimate, as specified by the rule above, works out to be 180 meters (about 25 times the array length). If we use typical dimensions for a towed array, the maximum range value for this scenario would equal approximately 5 kilometers.

93

This maximum range rule for 0.0 dB SNR must be considered in light of the design limitations of our computer simulation (see Section III). Assuming that we have a computer system with more available resources (CPU's), we could increase two significant values: the number of time samples taken per element over the data record length, and the number of elements in the receive array. Our research has shown that by increasing the number of samples, our location estimates improve. With more elements, the array would be larger, thereby improving the detection of wavefront curvature. Additionally, with more elements, the performance of the signal processing model is enhanced. One direct result of increasing these two parameters is an increase in the maximum estimation range determined by the algorithm. Our research has shown that the range estimate in a noise environment approaches the ideal no-noise result as we increase these parameters. Each test case conducted was validated to a range in excess of 100 kilometers for the no-noise condition.

In the course of our analysis the following topics for further research surfaced:

- Analyzing the performance of the localization algorithm in estimating target coordinates in an inhomogeneous medium.

- Development of a surface fi   ng routine to replace the non-linear least-squares estimation algorithm which only performs smoothing along the X and Y axes.

- Improving the performance of tne modified LMS frequency-domain adaptive algorithms or replacing these algorithms with other beamforming algorithms.

LIST OF REFERENCES

1. Ziomek, L. J. and Behrle, C. D., "Localization of Multiple Broadband Targets Via Frequency Domain Adaptive Beamforming for Planar Arrays," _The Journal of the Acoustic Society of America_, v. 85(3), pp. 1236-1244, March 1989.

2. Chan, F., _Two-Dimensional Beamforming Using a Frequency Domain Complex Least Mean-Squares (LMS) Adaptive Filter_, Master's Thesis, Naval Postgraduate School, Monterey, California, June 1986.

3. Temkin, S., _Elements of Acoustics_, John Wiley & Sons, Inc., New York, 1981.

4. Ziomek, L. J., "Course Notes for EC3450--Acoustic Field Theory," Naval Postgraduate School, Monterey, California, 1988.

5. Ziomek, L. J., _Underwater Acoustics, A Linear Systems Theory Approach_, Academic Press, Orlando, Florida, 1985.

6. Haykin, S., _Introduction to Adaptive Filters_, Macmillan Publishing Company, New York, pp. 90-126, 1984.

7. Wylie, C. R., _Advanced Engineering Mathematics_, McGraw-Hill Book Company, New York, pp. 130-134, 1966.

INITIAL DISTRIBUTION LIST

		No. Copies
1.	Defense Technical Information Center Cameron Station Alexandria, VA 22304-6145	2
2.	Library, Code 0142 Naval Postgraduate School Monterey, CA 93943-5002	2
3.	Chairman, Code 62 Department of Electrical and Computer Engineering Naval Postgraduate School Monterey, CA 93943-5000	1
4.	Chairman, Code 61 Ay Engineering Acoustics Academic Committee Naval Postgraduate School Monterey, CA 93943-5000	1
5.	Prof. L. J. Ziomek, Code 62 Zm Department of Electrical and Computer Engineering Naval Postgraduate School Monterey, CA 93943-5000	3
6.	Prof. J. H. Miller, Code 62 Mr Department of Electrical and Computer Engineering Naval Postgraduate School Monterey, CA 93943-5000	1
7.	Prof. Murali Tummala, Code 62 Tm Department of Electrical and Computer Engineering Naval Postgraduate School Monterey, CA 93943-5000	1
8.	Dr. Earl Messerre Technical Director Naval Underwater Systems Center Newport, RI 02481	1
9.	Dr. Duncan Sheldon Naval Underwater Systems Center Code 3314 New London, CT 06320	1

10. Dr. Rabiner Madan   1
    Office of Naval Research
    Code 1114
    800 N. Quincy St.
    Arlington, VA 22217-5000

11. Lt. R. P. Breckenridge, USN   2
    1572 Old Annapolis Rd.
    Arnold, MD 21012